SCHOOL OF ENGINEERING,

UNIVERSITY OF PATRAS,

COMPUTER ENGINEERING
AND INFORMATICS
DEPARTMENT

Whildfire Risk Assessment using Deep Learning Models and Images Captured by UAV's

Dissertation

Ilias Argyrakis

Supervising Professor: Emmanouil Psarakis

Patras, July, 2025

Acknowledgements

With the completion of this diploma thesis, my undergraduate journey also comes to an end. I would like to briefly thank all those who supported me along the way.

First and foremost, my professors, and especially my supervisor Professor Emmanouil Psarakis, whose guidance was invaluable in shaping the subject of this thesis and in making the most of my knowledge. His mentorship played a decisive role in my academic development.

I am also grateful to my friends: Iosif and Pelekan, whose advice was instrumental in the choice of my field of study and whose conversations greatly contributed to the smooth completion of my degree. Achilleas, Vasilis, Haris, Platon, and Philippos, who hosted me here and helped make my everyday life more pleasant and productive.

Finally, I would like to thank Adamantia and Dimos for the valuable memories we created during these years, as well as my parents for their unwavering support and trust in my abilities.

To all those mentioned, and to the many others not named, a heartfelt “thank you” for being part of this wonderful chapter in my life.

Abstract

This thesis presents the development of a prototype wildfire-risk mapping system based exclusively on imagery, both satellite and UAV-acquired.

First, a preliminary set of satellite images was assembled from the Google Earth collection, which was used to design and initially train convolutional neural networks. Next, a dedicated UAV dataset was created via drone flights, with meticulous annotation of the core classes (ground, shrubs, trees, roads, buildings, and high-voltage lines). Semantic segmentation was implemented using a U-Net architecture, while specialized mask post-processing techniques (thresholding, median filtering) ensured label quality.

Experimental results demonstrated high accuracy, satisfactory mean IoU, and robust performance in the most critical categories. Furthermore, we describe the procedure for assigning risk weights to each detected biomass type in order to produce the final "risk maps." The thesis concludes with a discussion of the challenges of real-time integration, as well as recommendations for expanding the dataset, incorporating 3D data, and deploying the system in full-scale field applications.

Table of Contents

Acknowledgements 2
Abstract 3
Glossary 6
Chapter 1 8
Introduction 8
1.1 The problem with wildfires in Greece 8
1.2 Methods of Confrontation 8
1.3 Gaps in Infrastructure 9
Chapter 2 11
Goals and Motives 11
2.1 Need for an Integrated System 11
2.1.1 Limitations of Satellite Images 11
2.1.2 Advantages and Limits of UAVs 11
2.1.3 Proposed Pipeline 11
2.2 Purpose and Research Questions 13
2.2.1 Purpose 13
2.2.2 Research Questions 14
2.3 Structure of the Thesis 14
CHAPTER 3 15
Theoretical Background / Related Research 15
3.1 Tree Cover in Greece 15
3.2 Which Trees Are More Dangerous 17
3.3 Why UAVs and not only Satellite Images 17
3.4 Semantic Segmentation 18
CHAPTER 4 21
Methodology 21
4.1 Training Using Satellite Images 21
4.1.1 Dataset Creation 21
4.1.2 Labeling 23

4.1.3 Working Environment, Processing & Data Augmentation 23
4.1.4 Neural Network Training 25
4.2 Training Using UAV Images 30
4.2.1 Limitations and Final Pipeline 30
4.2.2 Drone Design & Flight 31
4.2.3 UAV Dataset Class Creation & Labeling 32
4.2.4 Preprocessing & Augmentation 43
4.2.5 Training & Optimization 44
CHAPTER 5 46
Experimental Results 46
CHAPTER 6 57
Conclusion and Future Work 57
Bibliography 58
Appendix 62

Glossary

Satellite Image
Image of the Earth received from satellites in various spectra with specific spatial and temporal resolution.

Fuel Model
Description of types of biomass (e.g., dry grass, shrubs, cones) with characteristics used in fire spread prediction models (Rothermel, Scott & Burgan).

FARSITE
(Fire Area Simulator) — software for simulation of spread and intensity of forest fires based on topography, fuels and meteorological data.

BehavePlus
Fire behavior modeling system that allows prediction of spread rate, intensity and smoke production, based on various scenarios and fuels.

FWI (Forest Fire Weather Index)
Index of forest fire danger that derives from the Canadian Forest Fire Weather Index System, based on humidity, wind, temperature and rainfall.

UAV (Unmanned Aerial Vehicle)
Unmanned flying vehicle (drone) that can carry sensors and cameras for collection of high–resolution images.

Neural Network
Artificial intelligence model inspired by the function of biological neural tissue, capable of "learning" input–output relations through training on data sets.

Deep Learning
Subcategory of machine learning that uses "deep" (multi–layered) neural networks for automatic extraction of features from the data.

Semantic Segmentation
Image processing where each pixel is classified into one of the classes (e.g., forest vegetation, roads, buildings), providing accurate separation of regions of interest.

U-Net
Architecture of convolutional neural network for semantic segmentation with "encoder–decoder" layout and skip-connections, designed for medical images but widely adopted in geospatial applications.

Intersection over Union (IoU)
Evaluation measure of segmentation, the ratio of intersection (number of common pixels) to union (number of total pixels) between predicted and actual (ground truth) mask.

Ground Truth
The set of labels or reference maps defined "manually" by experts and used for training and evaluation of models.

Labeling
The process of assigning correct categories (classes) to images or pixels, either manually or with software assistance, for the creation of training sets.

Pipeline
The complete sequence of data processing from the collection of images to the final segmentation and the production of risk maps.

Script
The small code text or otherwise code segment, this structure is used in the google colab environment for the organized writing of code.

Accuracy
The percentage of correct predictions (true positives + true negatives) with respect to the total number of samples.

Precision
The percentage of correct positive predictions (true positives) with respect to all samples predicted positive.

Recall
The percentage of correct positive predictions (true positives) with respect to all actual positive samples.

F1-Score
The harmonic mean of Precision and Recall, which balances the two metrics.

Training / Validation / Test Set
The data subsets used respectively for training, parameter tuning and final evaluation of the model.

Data Augmentation
The technique of automatic creation of variations of the images (e.g., rotations, flips, change of brightness) to increase the variety of the training set.

Epoch

One complete pass of all samples of the training set through the network during training.

Chapter 1

Introduction

1.1 The problem with wildfires in Greece

Forest fires in Greece have taken on the dimensions of a national tragedy. In recent years, both their frequency and intensity have increased, driven mainly by:
• climate change,
• prolonged drought, and
• the uncontrolled accumulation of fuel material in forests.

In 2023, more than 174,000 stremmas of land were burned, while the total economic cost was estimated at approximately €1.8 billion [20]. At the same time, human losses ranged between 20–27 dead, with hundreds of families losing their homes and being displaced into temporary shelters [20].

The consequences extend beyond humans. Thousands of wild animals (deer, foxes, birds of prey) as well as domesticated ones (goats, sheep, horses, pets) either perished or were displaced into non-viable habitats [21]. Moreover, the destruction of vegetation led to soil erosion and a reduction in water resources, adversely affecting agricultural production and tourism in the long term [22].

Regarding hydrological impacts, large storm events occurring shortly after fires—such as *Storm Daniel* in September 2023—caused severe flooding in areas with burned vegetation, particularly in Thessaly. In just a few hours, more than 500 mm of rain fell, resulting in 16 deaths, the collapse of bridges and roads, and widespread crop destruction [23]. The agricultural sector was severely affected, as the fertile soils of the plain became unsuitable for cultivation for a considerable period.

1.2 Methods of Confrontation

The management of forest fires relies on four complementary phases: prevention, timely detection, behavior prediction, and suppression, followed by recovery and restoration after extinguishment.

Preventive measures
Fuel reduction through sanitation thinning, biomass management (fuel treatments),

and firebreak construction are based on Rothermel's "fuel models" [4] and are documented in the photo-guides of the 13 USDA fuel models [5].

Timely detection
Satellite systems such as MODIS and VIIRS cover large areas, but are limited by spatial resolution and revisit frequency [3]. The integration of UAVs with real-time or offline image processing techniques—as has been applied for vehicle detection in intelligent transportation [2]—enables the identification of small-scale fire spots.

Predictive behavior models
FARSITE [3] and BehavePlus [6] allow simulation of fire spread and intensity by incorporating:
• fuel,
• topography, and
• meteorological variables.

In parallel, the Fire Weather Index (FWI) provides continuous fire danger estimates based on weather data [8].

Suppression
Ground firefighting forces and aerial means (airplanes/helicopters) form the first line of defense but often face delays due to inaccessible terrain or low visibility.

Recovery & restoration
After suppression, erosion control works, reforestation, and monitoring of soil and hydrological impacts are undertaken to reduce risks from subsequent extreme weather events.

An integrated strategy requires incorporating all of the above into a unified information system that combines ground station data, satellite observations, and UAV imagery, supported by deep learning models for semantic segmentation of fire spots.

1.3 Gaps in Infrastructure

Despite extensive efforts in prevention and early detection, the Greek fire management system continues to exhibit critical shortcomings that increase risk and prolong response times.

The lack of adequate radar coverage and ground sensors means that existing meteorological station networks fail to cover the entire territory and are often located mainly in low-risk areas. As a result, the detection of new fire spots may be delayed by 8–12 hours [20].

The low spatial (250–500 m/pixel) and temporal (12–24 h) resolution of MODIS and VIIRS satellite imagery is insufficient for immediate intervention in small-scale forest areas [24], [25].

Even when recognition occurs in time, mobilization of aerial and ground resources is often delayed due to inaccessible terrain or the absence of suitable water sources. This results in valuable resources failing to reach the fire site promptly [20].

Micro–case study: In the area of Schinos, Corinthia, a dirt road used for rapid access had been filled in, forcing firefighting forces to take a 5 km detour. The resulting delay allowed the fire to double in size before it was extinguished [26].

These shortcomings highlight the urgent need for a unified, automated information system capable of integrating meteorological measurements, satellite data, and UAV high-resolution imagery in real time, combined with machine learning algorithms for accurate semantic segmentation and rapid fire danger assessment.

Chapter 2

Goals and Motives

2.1 Need for an Integrated System

2.1.1 Limitations of Satellite Images

Traditional monitoring of forest fires relies on satellite platforms such as Sentinel-2, which provides spatial resolution of 10 m and revisit times of 5–12 days. Although it offers broad coverage and long-term monitoring, the low level of detail does not favor the timely detection of small fire spots, while cloud sensitivity and relatively sparse acquisitions delay the response of services.

2.1.2 Advantages and Limits of UAVs

The use of UAVs (drones) allows image capture with spatial resolution on the order of cm–m and immediate time series in real time, facilitating the detection of even very small fire spots. However, flight range is limited, battery autonomy requires frequent landings, and field operation along with flight regulations impose increased organization and safety.

2.1.3 Proposed Pipeline

To address the above limitations, a system is proposed (see Figure 1) based exclusively on images. Initially, high-resolution UAV images are collected in priority zones, which are annotated with polygon masks to create a fully labeled dataset. Next, the images are fed into a semantic segmentation neural network (U-Net), trained to accurately separate different types of fuel biomass, roads, and infrastructures. After segmentation, the masks are processed through image analysis to generate risk maps.

In a subsequent phase, the system could integrate meteorological metadata, such as indices produced by the RiskMap platform of the Beyond EO Center, to create more holistic, dynamic risk maps, examples of which are illustrated in Figure 2 and Figure 3.

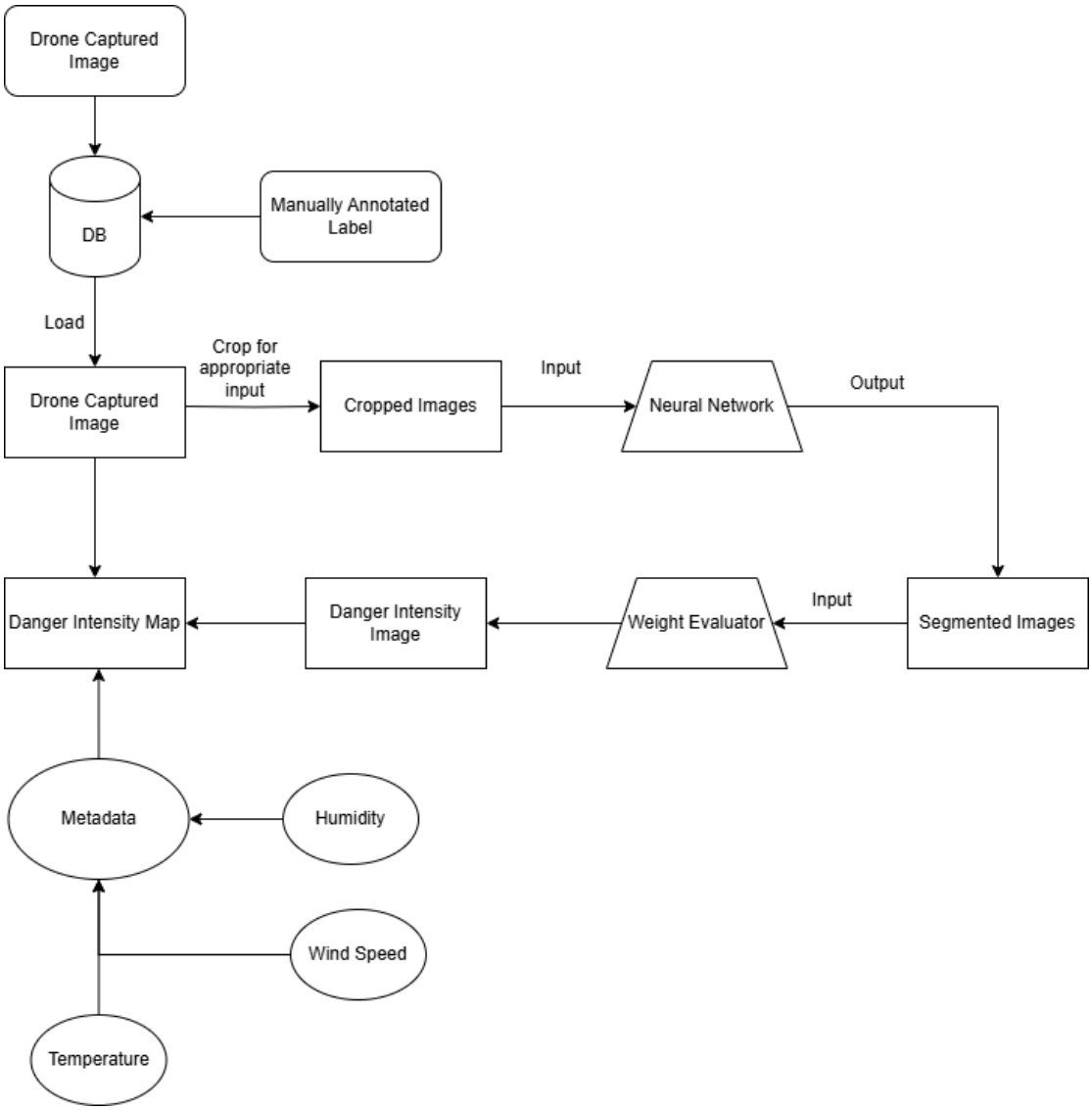

Figure 1: Proposed Pipeline.

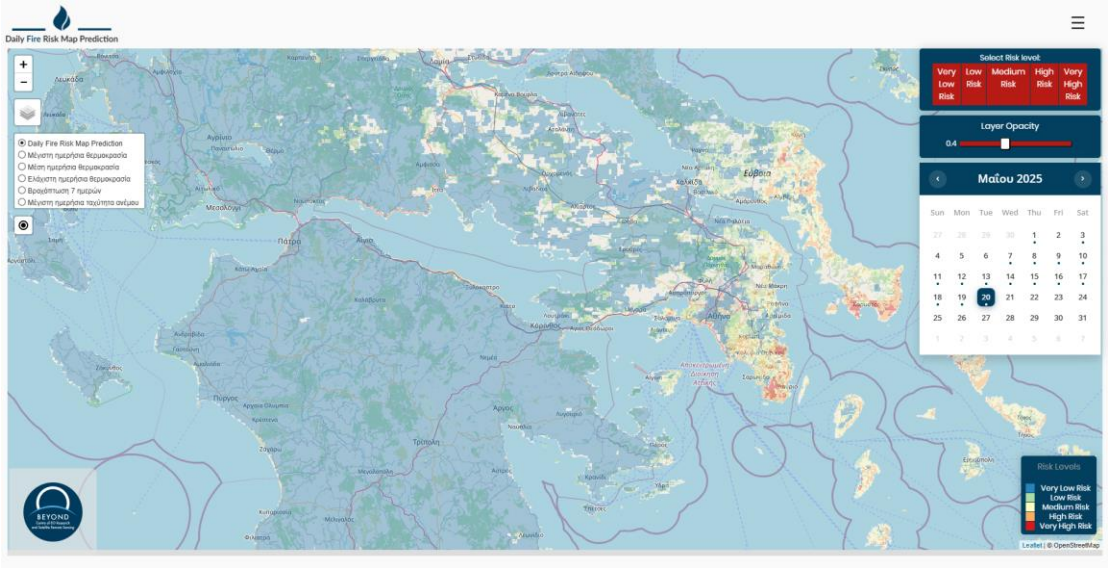

Figure 2: Wildfire Risk Assessment Examples from Firehub.

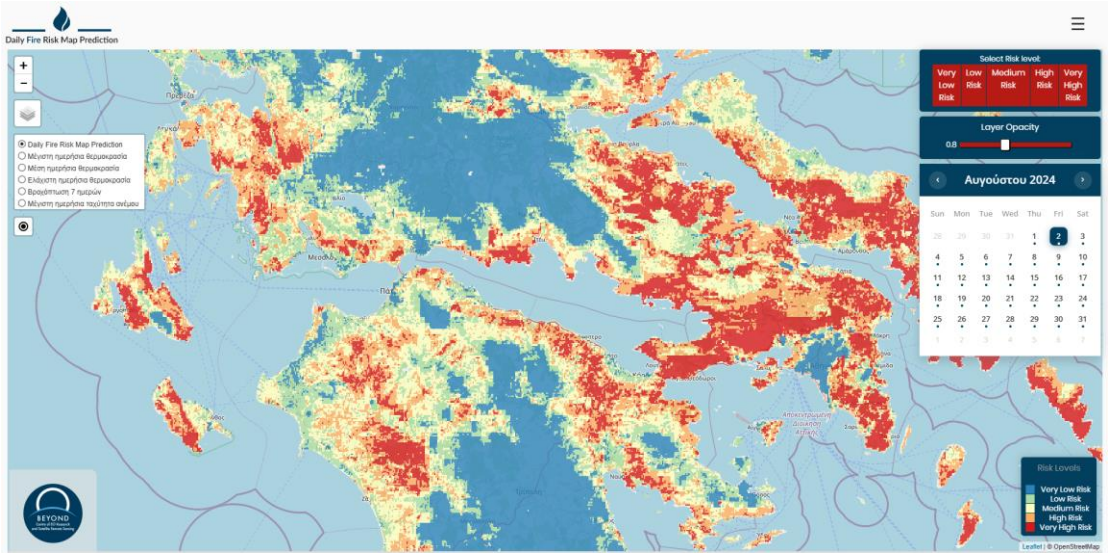

Figure 3: Another Example from a high Risk Measurement.

2.2 Purpose and Research Questions

2.2.1 Purpose

The main goal of this thesis is to investigate the feasibility of producing reliable wildfire risk maps using exclusively images and image processing/machine learning techniques. Emphasis is placed on enhancing detail in order to support both prevention and suppression, where firefighting units could consult integrated risk maps to combat and contain fires.

2.2.2 Research Questions

One way to make the objectives of this thesis more specific is by posing the following questions:

● Is it possible to generate a risk map with sufficient accuracy, comparable to manual reports (ground truth)?

● Which types of fuel biomass (image classes) have the greatest impact on shaping the risk index?

● How do spatial resolution and labeling quality affect model performance?

● To what extent does the level of class detail improve or slow down segmentation and the reliability of the generated maps?

These questions define the theoretical framework and guide the methodological development of the experiments that follow.

2.3 Structure of the Thesis

Chapter 3 ("Theoretical Background/Related Work") presents a review of forest areas in Greece, vegetation types and flammability parameters, as well as an introduction to the basic principles of semantic segmentation and the U-Net architecture.

Chapter 4 ("Methodology") describes the overall solution: the collection of satellite and UAV images, the design and labeling of the datasets, the selection of classes and acquisition conditions, preprocessing and augmentation of images, the implementation and analysis of neural networks for segmentation, and the assignment of risk indices.

Chapter 5 ("Experimental Results") reports the key performance metrics (accuracy, mean IoU, F1-score) and compares them with the ground truth.

Chapter 6 ("Conclusions and Future Work") summarizes the main findings, notes the limitations of the study, and proposes improvements for full integration in a real-time field environment.

The Appendix includes the main scripts and listings, while at the end the bibliography used is provided.

CHAPTER 3

Theoretical Background / Related Research

3.1 Tree Cover in Greece

At a national level, forest areas covered about 30.3% of the country's total land area in 2022, increased from 25.6% in 1990 and 30.3% in 2010 [27], [28]. This positive trend is mainly attributed to reforestation programs and natural regeneration, despite losses of forest land due to urban sprawl and uncontrolled grazing [27].

The main geographic forest zones and dominant species are [29]:
● Coastal and semi-rural areas (0–400 m): dominated by conifers such as *Pinus halepensis* (Aleppo pine) and maquis (*Quercus coccifera*).
● Mountainous core (400–1 200 m): dominated by *Pinus nigra* (black pine), *Fagus sylvatica* (beech) and *Abies cephalonica* (fir).
● Mediterranean shrublands and mixed broadleaves (0–800 m): strong presence of *Quercus ilex* (holm oak) and *Castanea sativa* (chestnut), particularly in the Ionian zone and the northern Aegean.

In total forest cover, conifers represent about 38%, while broadleaves account for 62% [27].
The distribution of forest cover and vegetation types is illustrated in the vegetation map of Greece shown below (see Figure 4). This map depicts, through color differentiation, the dominant vegetation species across the country, based on geographic, climatic and altitudinal characteristics.

In northern and northwestern Greece, such as Epirus, Macedonia and Thrace, there is a strong presence of dense deciduous and mixed forests, with dominant species including beech (*Fagus sylvatica*), fir (*Abies borisii-regis*, *A. cephalonica*) and black pine (*Pinus nigra*). These regions are characterized by high altitude and greater humidity, which favors the development of broadleaved species.

In central and southern mainland Greece, Mediterranean vegetation types dominate, such as maquis, phrygana shrublands and low bushlands, as well as stands of *Pinus halepensis* (Aleppo pine), mainly in lowland and coastal altitudes. The Peloponnese,

Attica, Euboea and Thessaly show extensive areas with mixed stands of pine and broadleaves, often interspersed with agricultural zones and infrastructure.

In island regions, such as the Aegean islands and Crete, vegetation shows greater heterogeneity. The dry and hot conditions favor mainly shrub vegetation, although in semi-mountainous zones clusters of cedars (*Juniperus* spp.), broadleaved oaks (*Quercus* spp.) and local chestnut groves can be found, such as in northern Euboea and Samos. In Crete, typical Mediterranean ecosystems are observed, with strong presence of phrygana, maquis vegetation and Aleppo pine in the east.

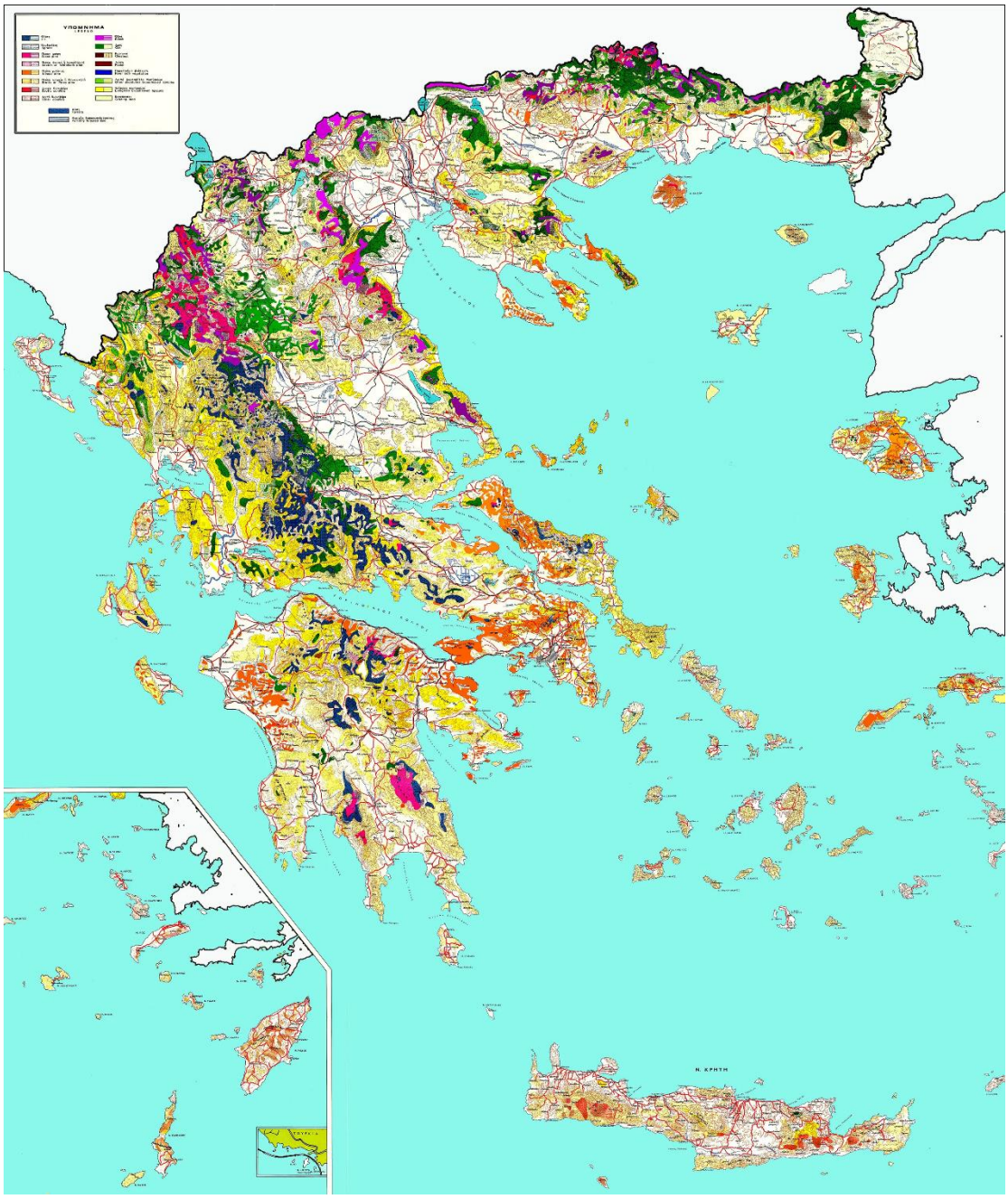

Figure 4: Map that showcases the distribution of tree species in Greece.

3.2 Which Trees Are More Dangerous

The flammability of trees is determined by a series of physiological and chemical characteristics that affect both ignition time and the rapid spread of fire. First, the Fuel Moisture Content (FMC), i.e., the water content of wood and needles/leaves, significantly prolongs ignition time when it is high, while low FMC values lead to faster fire spread [1].

The surface-to-volume ratio (SA/V) and the Specific Leaf Area (SLA) are indicators of the surface exposed to the atmosphere per unit of mass. Larger SA/V and SLA values imply increased oxygen access to the fuels, reduced ignition time and faster burning [1].

Leaf and bark thickness affect ignition time and burning rate, since thicker leaves require more heat to reach ignition temperature, while thicker bark slows flame progress and reduces annual biomass loss [16].

The volume and bulk density of leaf litter determines aeration. Low density creates an open structure that favors oxygen flow, enhancing ignition and fire spread [15].

The chemical composition of leaves (especially terpene and lignin content) also defines flammability: high terpene and non-structural carbohydrate content accelerates ignition and intensifies burning [16], [15].

In laboratory tests with "litter beds," *Pinus pinea* showed complete (100%) ignition success both in point-ignition and lateral fire-line tests, while *Cupressus sempervirens*, *Quercus ilex*, *Juniperus thurifera* and *Quercus faginea* showed success rates below 20% or even zero ignition [15].

In summary, conifers—especially species of the *Pinus* genus—rank high on the flammability scale due to low FMC and rapid spread in open litter beds. In contrast, some broadleaves such as *Quercus ilex* show reduced ignition susceptibility thanks to their thicker, lignin-rich leaves, although they sustain flames for longer once ignited. Species of the Cupressaceae family (e.g., *C. sempervirens*) take more time to ignite, but when they do, they produce high temperatures and prolonged burning.

3.3 Why UAVs and not only Satellite Images

Satellite images offer significant advantages in terms of wide coverage and continuous time series, but they present critical limitations for detecting and preventing micro-scale wildfire outbreaks. Specifically:

• Sentinel-2 provides spatial resolution of 10 m (while some spectral bands reach 20 m or 60 m), meaning that areas smaller than 10 × 10 m are not recorded in detail [30], while

• MODIS images have even lower resolution (250 m, 500 m and 1 km), making timely detection of small outbreaks impossible before they grow large [31].

Regarding temporal refresh:
• Sentinel-2's revisit cycle (about every 5 days, due to satellites 2A and 2B) is not sufficient for rapid response to events that unfold within hours, while
• MODIS completes global coverage every 1–2 days, creating windows during which new outbreaks remain unseen [30].

As a result, the lack of immediate detection of small outbreaks leads to delayed mobilization of firefighting forces and a higher risk of losing control over suppression.

In contrast, UAVs (drones) provide spatial resolution reaching cm or m levels, enabling detailed biomass mapping and rapid hotspot detection in real time. Their flight flexibility—targeted missions over critical zones, independent of clouds or topographic constraints—and the possibility of repeated flights at short intervals further enhance early detection [2]. Moreover, the lower initial investment and operational costs compared to subscription-based high-resolution satellite imagery make UAVs an excellent complement to traditional satellite monitoring.

Application examples, such as vehicle detection in intelligent transportation [2] and crop monitoring in precision agriculture [17], highlight the wide processing capabilities of drone imagery. Therefore, the use of UAV images effectively complements the gaps of satellite coverage, addressing small-scale surveillance needs and strengthening early intervention against wildfires.

3.4 Semantic Segmentation

Semantic segmentation aims at classifying each pixel of an image into a predefined class, producing a dense mask map that shows exactly:
• which areas belong to forest vegetation,
• which to roads or man-made infrastructure, and
• which to dead organic matter.

The idea of Fully Convolutional Networks (FCNs), as proposed by Long, Shelhamer & Darrell (2015), was to replace traditional fully connected layers with convolutional ones so that the network could output predictions at dimensions corresponding to the input, preserving spatial information.

Although the first FCNs gradually reduced dimensions through pooling and lost detail, the U-Net architecture (Ronneberger, Fischer & Brox, 2015) addressed this issue with a symmetric encoder–decoder scheme and "skip connections" that transfer fine details from the down-sampling stages to the corresponding up-sampling stages.

In this way, each decoder layer receives both the compressed features from the encoder and the original high-resolution details, achieving sharper boundaries between classes and significantly improving contour accuracy (see Figure 5).

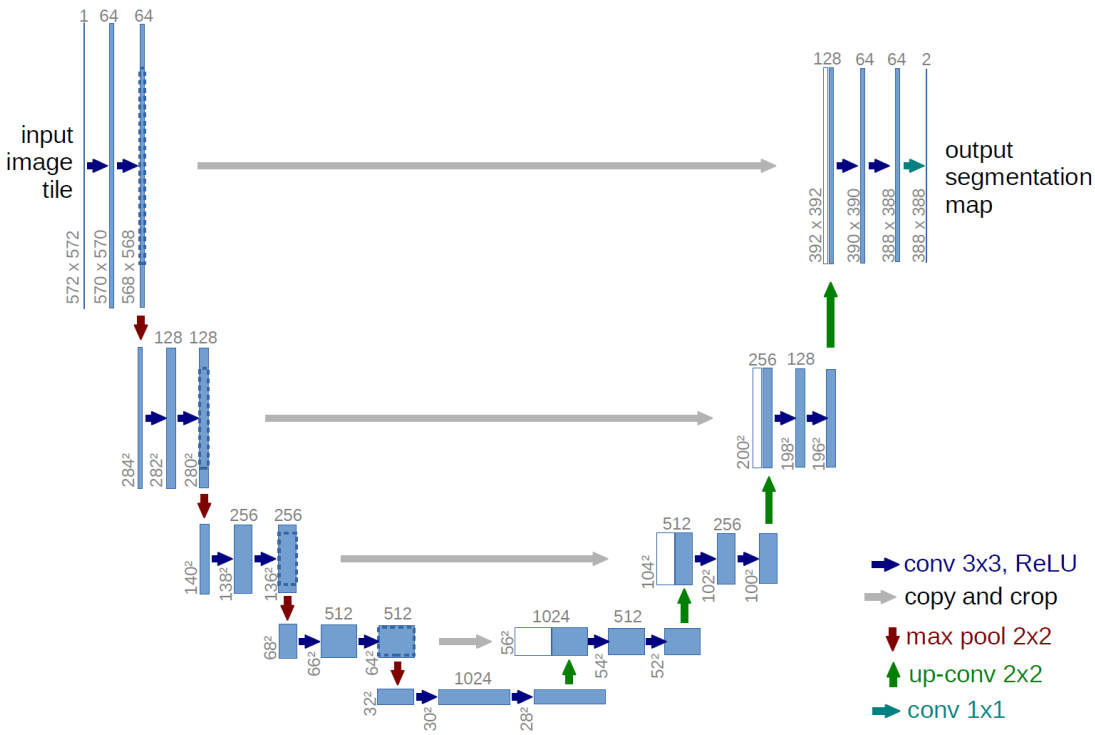

Figure 5: U-Net Architecture.

In geospatial applications, semantic segmentation enables:

- the separation of land cover types,
- accurate estimation of biomass (forests, shrubs, grasslands), and
- rapid identification of man-made features such as roads and buildings,

making it possible to create a risk map based on the presence of fuels or access points.

The main performance metrics, Intersection over Union (IoU), Pixel Accuracy, and F1-Score, respectively measure the overlap between predicted and ground truth masks, the overall proportion of correctly classified pixels, and the balance between false positives and false negatives, ensuring that the model neither overemphasizes nor overlooks critical classes.

The choice of U-Net in this thesis is based on its proven effectiveness when trained on relatively small datasets, thanks to the skip connections that preserve spatial details, as well as its flexibility to process fixed-size patches (e.g., 256×256) without losing coherence in the output. Once the mask is generated, each pixel label is mapped to a risk index, weighted according to the importance of its class, and ultimately combined into a map that highlights hazardous zones requiring attention.

CHAPTER 4

Methodology

4.1 Training Using Satellite Images

4.1.1 Dataset Creation

For training the semantic segmentation models, it was necessary to gather a representative set of satellite images that capture different forest conditions while avoiding images with disturbances (clouds, snow, or excessive urban areas). The process followed these steps:

Image Sources
Satellite imagery was obtained from Google Earth, a highly detailed mapping platform (see Figure 6). The image resolution corresponds to 50 m/pixel, making it computationally feasible to extract images that adequately represent the study area.

Class Selection & Assumptions
The labels from the ImageCollection *GOOGLE/DYNAMICWORLD/V1* include the following classes:

- Water
- Trees
- Grass
- Flooded Vegetation
- Crops
- Shrub
- Built-up Area
- Bare Area
- Snow & Ice
- Clouds

For this specific application, more data was collected from classes directly related to vegetation. Consequently, classes such as (8) Snow & Ice and (9) Clouds provide limited qualitative value compared to vegetation-related classes like (1) Trees.

To ensure dataset quality and focus on clean, summer conditions, the following criteria were applied:

1. Minimum cloud coverage < 10% per image (filtered using the metadata field *CLOUDY_PIXEL_PERCENTAGE*).

2. Low soil moisture (summer period, June–September).

3. Exclusion of snow-covered or flooded areas, ensuring at least 30% of pixel classes belong to class 1: Tree.

4. Random sampling within the central zone of Greece (geographical range Kalamata–Thessaloniki) using a Gaussian distribution. By multiplying the coordinate variables with a random variable drawn from a Gaussian distribution, a variety of altitudes and vegetation types could be covered.

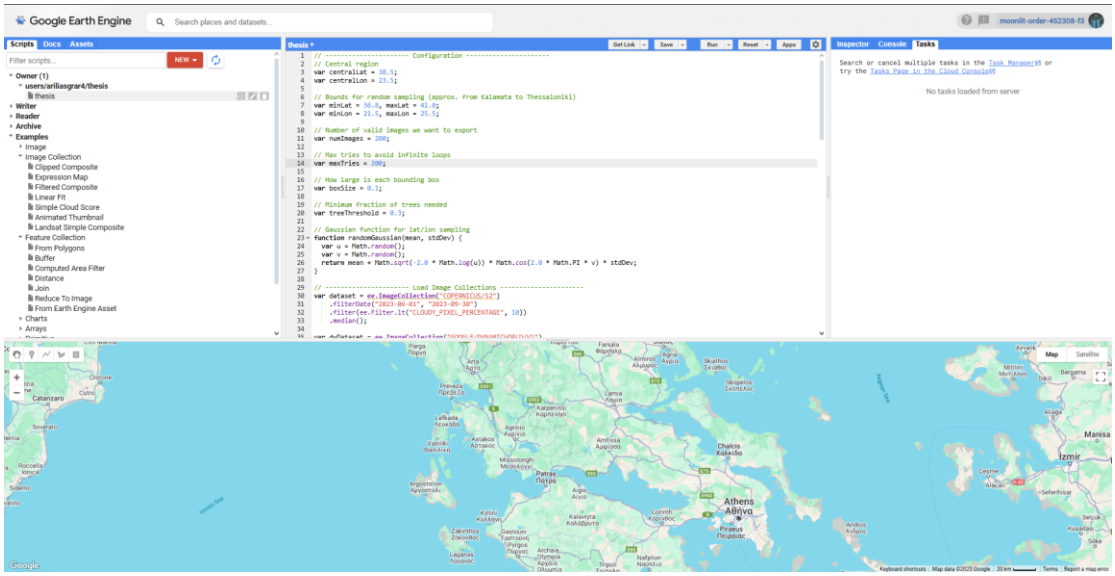

Figure 6: The IDE of Google Earth.

The full script (Listing 1) that implements the sampling and extraction of images from Google Earth Engine is included in the Code Appendix, ensuring reproducibility of the process and the extraction of exactly 200 images, each with a size of 446×446 pixels (height and width), with at least 30% forest cover.

4.1.2 Labeling

In Google Dynamic World (DW), the labeling of Sentinel-2 images has already been carried out using an advanced convolutional neural network trained on large, high-resolution datasets where the "ground truth" labels were generated through expert manual annotation. Each pixel is classified into one of ten classes (e.g., water, trees, grass, built-up area, etc.), using features from the visible and infrared spectral bands.

For every Sentinel-2 image, the algorithm generates a label mask (*label = [0…9]*) per pixel based on Dynamic World data. However, before this output is used in the training set, it undergoes strict quality control. Specifically, random subsets of images are selected for visual inspection to detect and discard regions with unreliable predictions—such as confusion between water and clouds—while, where necessary, corrections are applied using post-processing rules (e.g., thresholding, majority filtering). In this way, the final masks remain clean and reliable, allowing the neural network to accurately learn the characteristics of forest vegetation and other categories without noise from mislabeled data.

The risk of mislabeling is therefore significant. For this reason, the use of a dataset labeled directly by humans is of critical importance. However, in images captured at such altitudes, this process is extremely difficult and time-consuming due to the low clarity of the depicted areas. This limitation does not apply to drone-based imagery, where the much higher resolution makes manual labeling both easier and more precise.

4.1.3 Working Environment, Processing & Data Augmentation

Google Colab served as the main environment for model development and training (see Figure 7), as it provides free access to GPUs (typically NVIDIA Tesla T4 or P100) and a preconfigured Python setup with packages such as TensorFlow, Keras, and Rasterio already installed. With the ability to connect directly to Google Drive, it was possible to seamlessly read and store both the original satellite GeoTIFF images and the generated patches, without requiring local uploads.

GPU acceleration in Colab significantly improved computational performance during training—both in the forward pass and the backward pass—reducing network training time per epoch from hours to just a few minutes. Despite the relatively limited memory (around 12–16 GB VRAM) and the maximum continuous runtime (about 12 hours), Colab is considered an ideal platform for research and experimentation, as it combines flexibility, collaboration (easy notebook sharing), and immediate access to high-performance computational resources.

Figure 7: IDE of Google Colab.

After the initial extraction of the satellite images, each image was normalized so that pixel values ranged within [0, 1]. Normalization was performed through simple linear shifting and scaling, using the following relation:

$$arr = (arr - arr.min()) / (arr.max() - arr.min() + 1e\text{-}8)$$

to prevent the creation of "dead" pixels when the value range was too small. Additionally, histogram matching was applied using the function skimage.exposure.match_histograms, in order to align the intensity distribution of each image with that of a selected reference image. This ensured homogeneity across images originating from different dates or sensors, reducing lighting variations and the risk of noise during network training.

Since the extraction and storage of the first 200 clean images from Google Earth Engine proved to be particularly time-consuming, it was decided not to further expand the initial dataset with additional downloads. Instead, data augmentation and cropping techniques were applied to enrich the available data. Specifically, each image underwent:

- random rotations of up to ±15°,
- horizontal and vertical flips,
- moderate brightness adjustments, and
- contrast modifications (±20%).

After augmentation, each image was divided into sliding window crops of 256×256 pixels with a stride of 50 pixels, keeping only those patches that contained at least

25% forest cover. This approach multiplied the number of samples without additional acquisition cost and ensured the U-Net was consistently fed with thousands of suitable patches for training.

4.1.4 Neural Network Training

For training the U-Net architecture, which is characterized by a symmetric encoder–decoder structure with five downsampling and upsampling levels, the following design was used. In the contracting path, successive pairs of convolutional layers (Conv2D) with 3×3 kernels and ReLU activation were applied, starting from 64 filters at the first level and doubling at each encoder step (128, 256, 512) until the bottleneck, where 1024 filters were used. Each pair of convolutional layers was followed by a 2×2 max pooling operation, halving the feature map dimensions and condensing higher-level information.

In the expansive path, the inverse process was implemented with transposed convolutions (Conv2DTranspose), which doubled the spatial dimensions, while skip connections concatenated the corresponding encoder feature maps. This ensured that fine-grained spatial information remained available up to the final layer.

Hyperparameter tuning included the Adam optimizer with default learning rate (0.001), while both batch size and number of epochs were adjusted for efficiency. The network was trained for 50 epochs with a batch size of 8, as this combination allowed for rapid convergence without excessive GPU memory consumption. Training progress was monitored through the loss function (*sparse_categorical_crossentropy*) and accuracy metrics on both training and validation sets, enabling early detection of potential overfitting.

Performance evaluation employed a custom metric, Mean Intersection over Union (*mean_iou_9*), which computed the average IoU across the nine available classes. Additionally, after training completion, F1-Score, precision, and recall were calculated for each class to assess the balance between false positives and false negatives. Finally, overall Pixel Accuracy confirmed that more than 83% of pixels were correctly classified in the test set, while the mean IoU approached 0.41, providing a reliable basis for the construction of risk maps.

During training, the GPU resources of Google Colab were used, enabling batch image processing and significantly accelerating both the forward pass and the backward pass. This allowed the completion of 50 epochs in relatively short time, without the need for high-end local hardware.

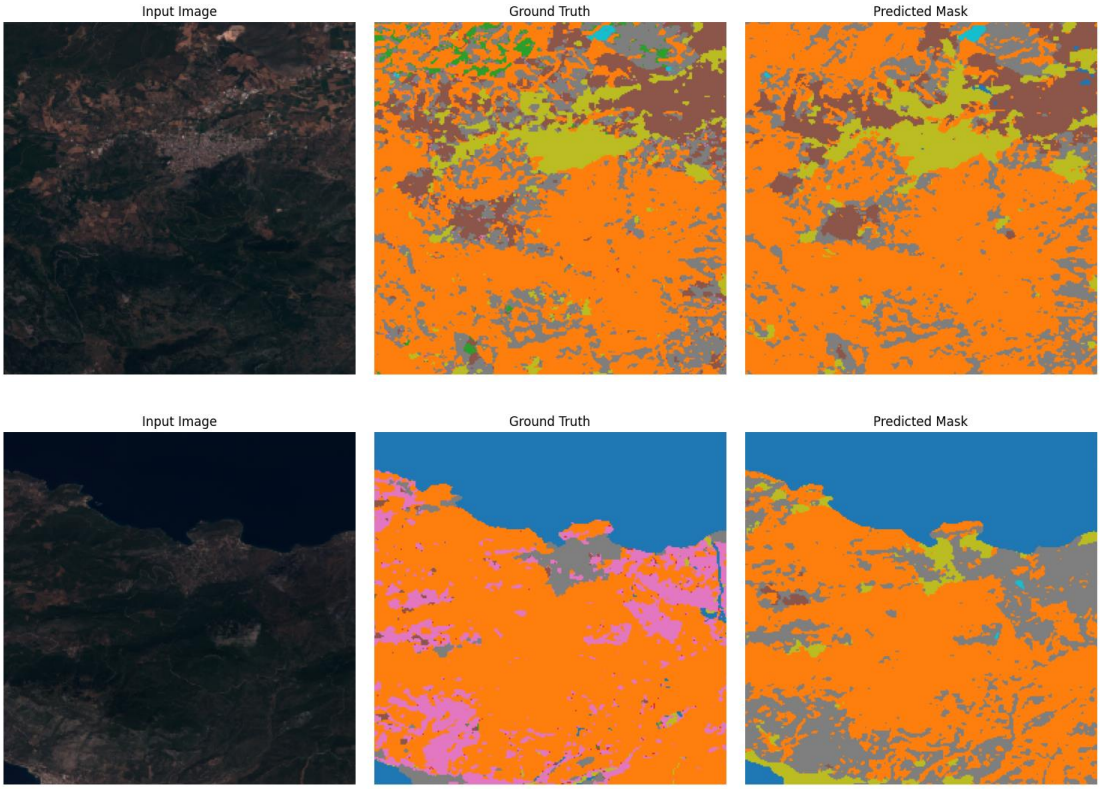

Figure 8: Examples of Neural Network training on satellite images.

Several examples from the training process are presented in Figure 8. Overall, the model demonstrated very good performance and showed that it could predict images with encouraging accuracy. In the figure, for instance, the left column displays random land areas from regions of Greece, the middle column shows the corresponding ground truths, and the right column depicts the model's predictions.

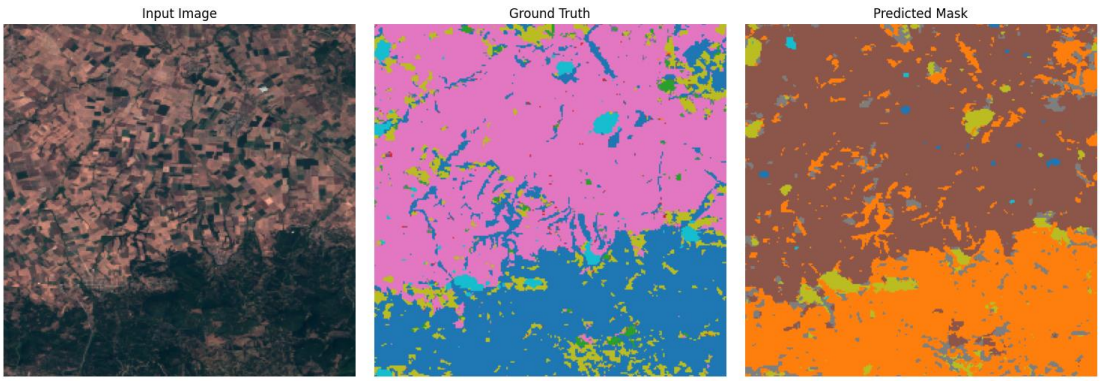

Figure 9: Unique Example.

In Figure 9, we can observe a special case in which, although the data are incorrectly labeled (for example, the water class in blue appears over a clearly forested area), the

U-Net still manages to classify the regions correctly thanks to the robustness it developed during training. This serves as an example of machine learning emerging as a cutting-edge technology.

In Graph 1 of Figure 10 ("Distribution of Precision Across Classes"), we observe that class 0 (Water) achieves the largest share of precision, while class 8 (Ice) is nearly absent due to the choice of images from Greek terrain during the summer season—consequently, this category is not predicted correctly. The classes "Trees" (1) and "Shrubs" (5) show high precision values, indicating that when they are predicted, their accuracy is satisfactory. In contrast, the classes "Grass" (2) and "Flooded Vegetation" (3) exhibit lower precision, signaling that they are often confused either with each other or with the background ("Ground").

In Graph 2 of the same figure ("Distribution of F1-score Across Classes"), the F1-score unifies precision and recall. Here, class 0 still dominates, while classes (1) and "Crops" (4) also demonstrate a good balance between false positives and false negatives. Classes (2) and (3) maintain medium-to-low values, highlighting the need for improved sampling or targeted augmentation steps for these specific categories.

Finally, Graph 3 ("Distribution of IoU Across Classes") reveals that class (0) achieves the highest IoU score, followed by class (1), while classes (8) and (2) appear at the lowest end. This indicates that the network performs well on classes related to the main problem, while for the remaining ones, the dataset lacks sufficient representation.

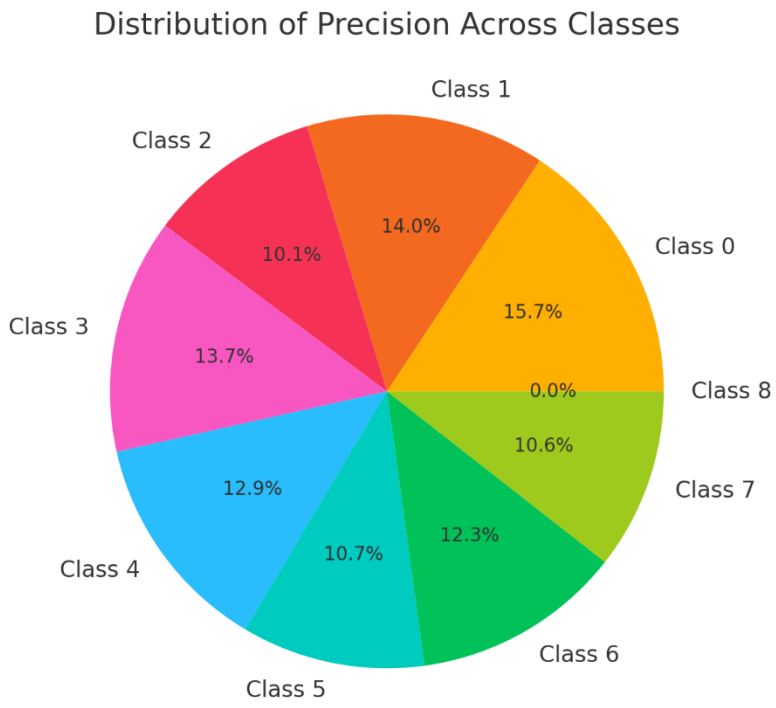

Graph 1

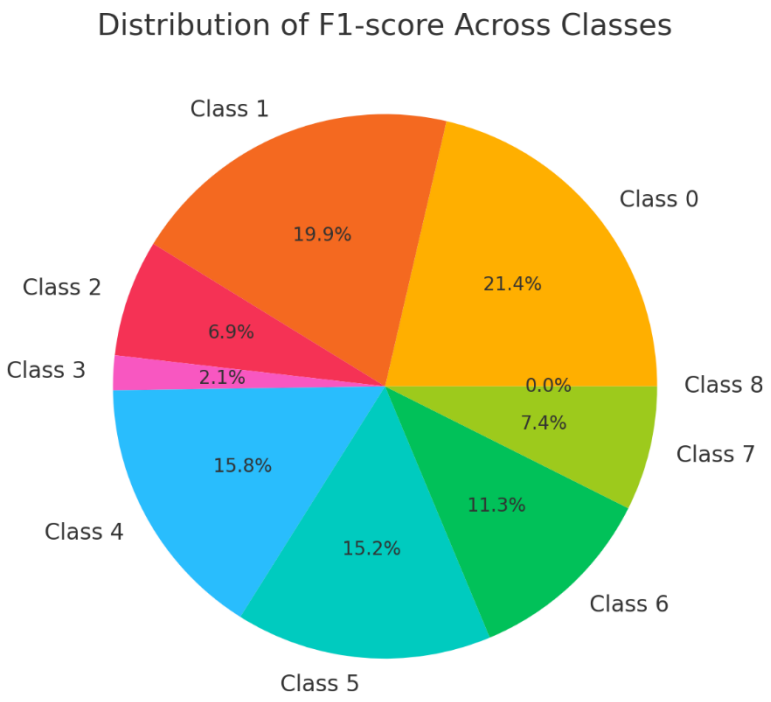

Graph 2

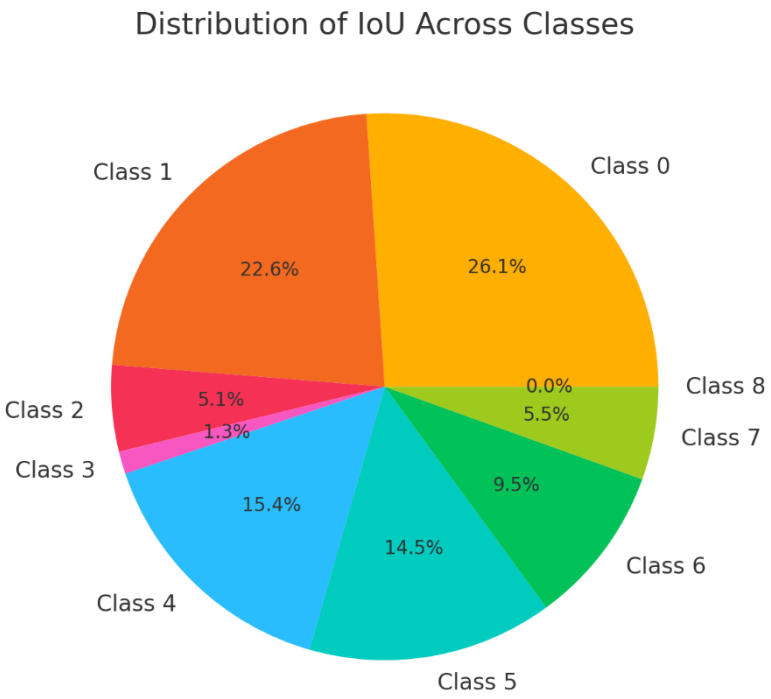

Graph 3

Figure 10: Results of Training in Graphs.

These visualizations facilitate class-wise comparison and the identification of which objects the network performs better or worse on, thereby supporting decisions for improving and refining the dataset.

The core code is provided in the Code Appendix (Listing 2). No further emphasis will be placed on the satellite image training component, as this stage primarily served as a means of gaining familiarity with U-Net and training procedures in general. Consequently, the focus shifts to UAV images, which form the foundation of this thesis.

4.2 Training Using UAV Images

4.2.1 Limitations and Final Pipeline

During the implementation of the proposed system, several critical hardware and software limitations were identified, the resolution of which would significantly enhance the quality of the results. First, the available drone did not support an onboard code development environment nor did it possess sufficient computational power for real-time image processing—limitations arising from the rapid evolution of batteries and firmware in recent years. As a result, it was not possible to execute automated flight plans with constant altitude differences or to adapt the field of view in real time. The altitude parameter, crucial for consistent vegetation resolution, was instead introduced empirically during labeling, affecting the dataset's homogeneity.

Furthermore, the lack of prior experience in labeling led to errors in the initial annotations. Despite correction attempts through post-processing (thresholding, median filtering) and random quality checks, some mistakes persisted and measurably impacted performance metrics.

Finally, limited computational resources—restricted GPU memory and execution time—necessitated the use of a relatively small training set, reducing sample diversity and constraining model complexity. Increased computational availability and the adoption of distributed training techniques would enable the use of larger datasets and more demanding architectures, leading to further improvements in both accuracy and generalization.

The illustrated pipeline in **Figure 11** begins with capturing high-resolution images from the drone, which are stored locally for further processing. Each full image is then cropped into smaller patches to match the input size requirements of the neural network.

Next, the patches are fed into the trained semantic segmentation model (U-Net), which assigns a class label to each pixel (e.g., ground, bush, big tree, etc.). These masks are subsequently reassembled into their original geographic layout to reconstruct the full segmented image.

The following stage involves risk evaluation: each class label is assigned a predefined risk weight, and a simple evaluator computes the "risk intensity" per pixel. The result is a **danger intensity map**, which visualizes the most hazardous zones with graded color scales.

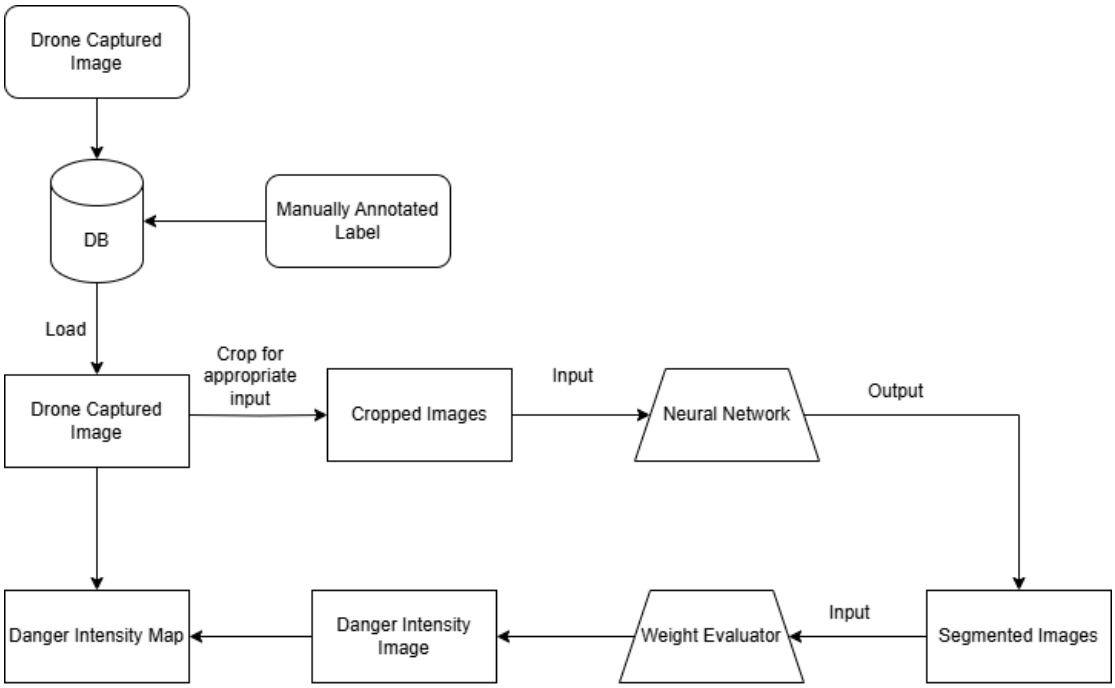

Figure 11: The implementation of the pipeline.

4.2.2 Drone Design & Flight

For UAV image acquisition, the DJI Phantom 4 Pro model was selected (see Figure 12), which does not require special operator certification for flights within university premises. All flights were restricted to the campus area and conducted at an altitude of 100 m in order to comply with applicable regulations. The integrated 1″ CMOS camera with a horizontal field of view of approximately 84° captured a ground swath of about 180 m at the horizon. With a horizontal image resolution of 5,472 pixels, this corresponds to a spatial resolution of approximately 3.3 cm/pixel (Ground Sampling Distance). Each pixel therefore covers an area of about 0.001 m², ensuring sufficient detail for subsequent semantic segmentation (Figure 12).

Despite the high image quality (20 MP) and flight stability, the platform does not support onboard processing beyond basic video recording; all segmentation and labeling operations were instead performed offline in a workstation environment. Data management via the DJI SDK presents limitations in live stream transmission (latency, frame loss) and requires complex synchronization between the code and the ground station.

The mission design included a flight path width of 60 m (due to licensing restrictions), a flight altitude of 100 m, and an overlap >70% both horizontally and vertically, ensuring adequate redundancy for orthomosaic stitching and consistent coverage. Additional considerations included flight duration (~27 minutes per battery), the spring season for vegetation with rich color diversity, midday flights to

minimize strong shadows, and weather constraints (winds up to 5 m/s). Together, these factors ensured stable image quality and a smooth data flow for the subsequent stages of the methodology.

Figure 12: DJI Phantom 4 Pro Drone.

4.2.3 UAV Dataset Class Creation & Labeling

As part of the data collection process, a total of 100 images were captured, ensuring sufficient variety in lighting conditions. From these, ten images were selected for manual labeling (see Figure 13) due to their rich content in vegetation and infrastructure classes. Their relatively large size allowed the creation of 2,520 image patches with dimensions of 256×256 pixels, which directly served as input to the U-Net.

Although this volume of samples was adequate, the limited computational resources, specifically GPU memory availability and training time on Google Colab, restricted the training to smaller batch sizes and fewer epochs. As a result, the training experiments could not fully leverage hyperparameter optimization and ultimately yielded suboptimal performance metrics.

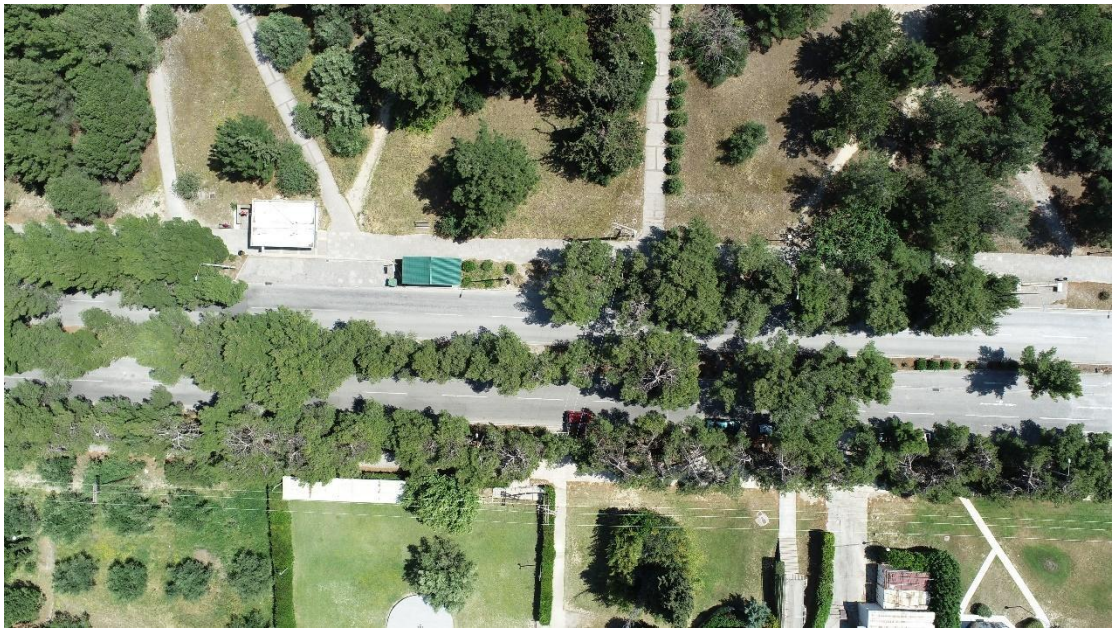

Figure 13: Image Example captured by the Drone.

Labeling Classes for UAV Imagery

Seven labeling classes were defined, reflecting both the fire hazard and the functional significance of vegetation and anthropogenic elements in wildfire-prone landscapes:

Ground & Substrates (ground)

The *Ground & Substrates* class (see Figure 14) includes bare soil often covered with fine layers of dry grasses, pine needles, bark, and branch residues. Although these are not considered "heavy" fuels, they act as ignition triggers and "bridges" for fire spread. Such fine fuels exhibit low moisture content and high surface-to-volume ratios, which significantly reduce ignition time and accelerate flame propagation across the vegetation layer. Additionally, slope and soil texture affect fire spread rate: uphill slopes accelerate propagation, while compacted substrates, such as dirt roads or firebreak zones, slow down transmission and may serve as partial natural barriers.

Figure 14: Example of Class ground.

Accurate recognition and mapping of this class via semantic segmentation enables detailed representation of areas where ground conditions contribute to initial spread, guiding targeted clearing operations for fine fuel removal and assessing the effectiveness of existing firebreaks.

Shrubs & Grasses (bush)

The *Shrubs & Grasses* class encompasses low- to medium-height shrub vegetation (e.g., broom, mastic shrubs, asparagus scrub) as well as dry grasses forming dense mats (see Figure 15). This structure combines high volumes of dry plant matter with elevated surface-area-to-volume ratios, promoting rapid flame spread. The mixture of green and dry elements creates zones of variable flammability, where ignition often starts in dry grasses before flames are carried into denser shrubs. In peri-urban and semi-rural areas where vegetation clearing is difficult, accurate segmentation of this class supports prioritization of regions for fuel treatment and timely activation of preventive measures.

Figure 15: Example of Class bush.

Medium-Risk Trees (mid tree)

The *Medium-Risk Tree* category includes species such as cypress and olive trees (see Figure 16). Despite their considerable height, cypress trees exhibit narrow crowns and high wood moisture, resulting in relatively low biomass volume and slow fire spread. Similarly, olive trees possess moderate height and canopy width, thick lignin-rich leaves, and medium stem density—all factors that lengthen ignition time and slow combustion rates.

Figure 16: Example of Class mid tree.

High-Risk Trees (big tree)

The *High-Risk Tree* category includes species with large biomass volumes and thin, flammable foliage or needles (see Figure 17). Typical examples are pine (Pinus spp.), where thin needles and resinous bark accelerate ignition and flame propagation, and eucalyptus (Eucalyptus spp.), whose leaves are rich in essential oils and whose thick layers of shed bark accumulate on the ground, forming highly combustible material. These characteristics make such trees critical accelerators in wildfire dynamics.

Figure 17: Example of Class big tree.

High-Voltage Electrical Infrastructure (electrical)

The *Electrical* class corresponds to substations, pylons, and power distribution lines, which represent critical nodes in fire hazard maps (see **Figure 18**). Tree branches approaching power lines significantly increase the risk of sparks or short circuits that may ignite fires. Furthermore, cable failure or damaged insulators may bring live wires into contact with combustible materials, greatly raising ignition likelihood under dry conditions. Systematic mapping of these infrastructures alongside surrounding vegetation enables early identification of *"high electrical hazard zones"* and the planning of preventive trimming or insulation assessments. In the final model, this class is recorded for hazard purposes but excluded from fire-spread modeling, since cables are not fuels themselves; rather, detection serves to prevent fire ignition or exacerbation due to electrical accidents.

Figure 18: Example of class electrical.

Roads (road)

The *Roads* class includes both paved and unpaved roads (see **Figure 19**). Roads act as potential firebreaks due to the absence of biomass on their surfaces, but also as key access routes for firefighting units. Accurate mapping supports optimal route planning and arrival-time estimation, while identifying locations where flames may "jump" across roads (e.g., steep slopes or planting gaps). Any object detected on the road surface or sidewalk (e.g., vehicles, bins, poles) is also categorized under *Roads*, to prevent misclassification as combustible vegetation and ensure reliable accessibility maps.

Figure 19: Example of class road.

Buildings & Man-Made Structures (building)

Η κατηγορία «Κτίρια & ανθρωπογενείς κατασκευές» λειτουργεί ανάλογα με την κλάση The *Roads* class includes both paved and unpaved roads (see Figure 19). Roads act as potential firebreaks due to the absence of biomass on their surfaces, but also as key access routes for firefighting units. Accurate mapping supports optimal route planning and arrival-time estimation, while identifying locations where flames may "jump" across roads (e.g., steep slopes or planting gaps). Any object detected on the road surface or sidewalk (e.g., vehicles, bins, poles) is also categorized under *Roads*, to prevent misclassification as combustible vegetation and ensure reliable accessibility maps.

Figure 20: Example of class building.

Annotation Process

UAV images were annotated using polygonal labeling in the VGG Image Annotator (see Figure 21), with particular care taken at class boundaries. This level of detail ensured accurate class distinction and preservation of object characteristics despite landscape complexity. The annotations were exported in JSON format. Each image required on average six hours of manual annotation and contained approximately 250 labeled regions, with pixel distribution across the defined classes.

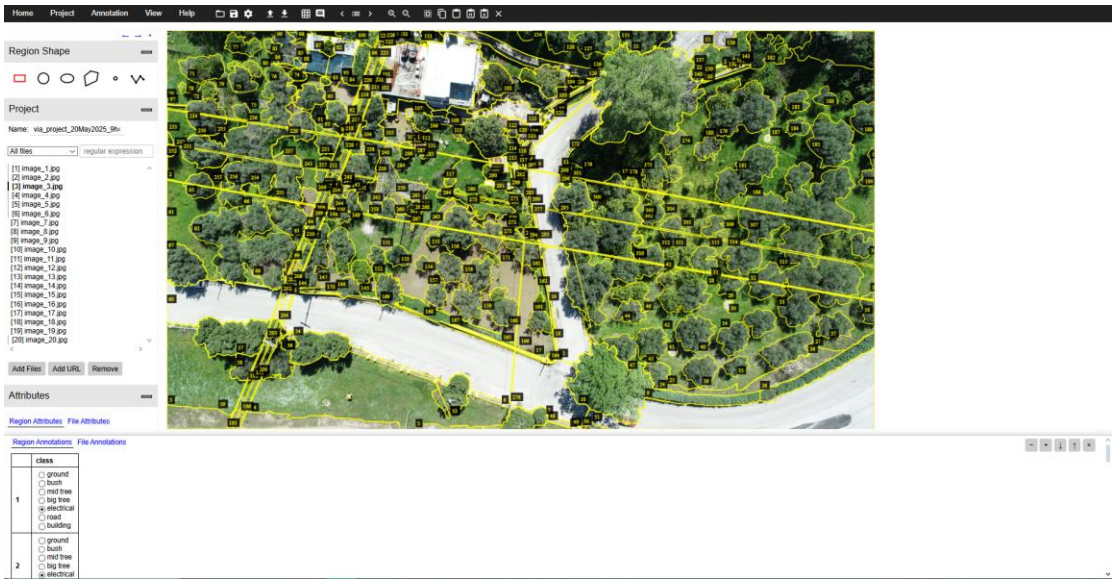

Figure 21: Annotating VGI IDE.

For the conversion of the labels from the JSON file into mask images, an automated script was used (see Appendix, Listing 3). After importing the exported VIA annotations, the script assigned each polygon region to its corresponding class using a predefined color map (e.g., *"ground"* → *red*, *"bush"* → *dark brown*). During this process, any gaps—pixels that did not belong to a region—were automatically filled using the nearest-neighbor method (Voronoi), ensuring that no empty zones remained in the final mask. Each mask was then saved in PNG format, preserving the geographical dimensions of the corresponding RGB image. This procedure produced masks ready for training, without the need for additional manual correction or post-processing.

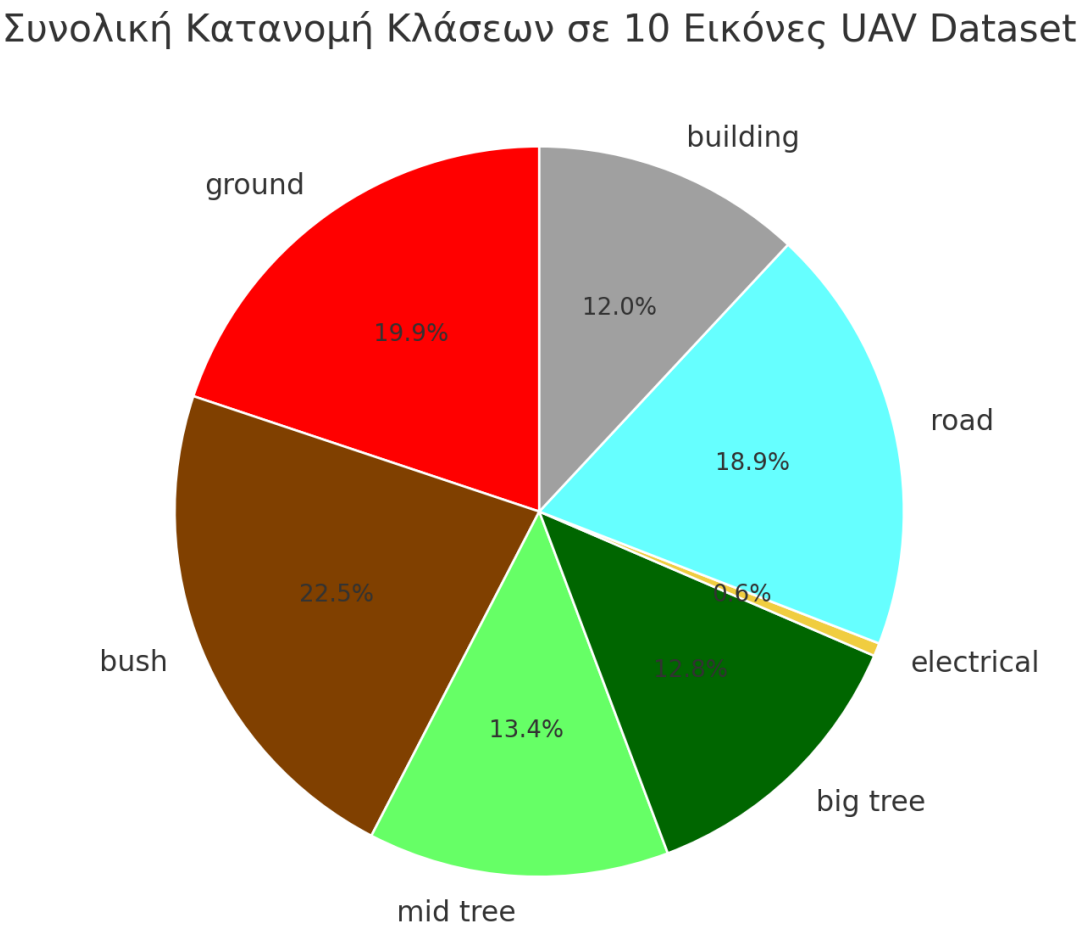

Graph 1

Figure 22: Distribution of the pixels of the classes.

The overall class distribution across the 10 UAV images, illustrated in Graph 1 (see Fig. 22), reveals significant imbalances. The largest share corresponds to “bush” (22.5%) and “ground” (19.9%), while “roads” account for 18.9%. “Medium-risk trees” and “high-risk trees” represent 13.4% and 12.8% respectively, and “buildings” reach 12.0%. In contrast, “electrical equipment” is nearly absent (0.6%), making it necessary either to artificially augment this class through data augmentation or to apply class weighting during training so that the model learns to detect it reliably. The relative underrepresentation of “big trees” (12.8%) compared to “bush” and “ground” also highlights the need for balanced sampling, especially if efficient detection of large trees is a key objective for fire spread prevention.

4.2.4 Preprocessing & Augmentation

To address the lack of high-risk tree (*big-tree*) samples in the original dataset, a balancing mechanism was applied during the train/val/test split. In total, 2,520 patches were generated, of which 704 correspond to the *big-tree* class and 1,816 to all other classes. The training set contained 2,085 samples (including 633 *big-tree*), the validation set 217 samples (35 *big-tree*), and the test set 218 samples (36 *big-tree*). This ensured that the network was exposed to sufficient variety and quantity of the most hazardous vegetation types, improving its ability to both learn and generalize their detection.
Given the dataset size (2,520 crops of 256×256 pixels), as shown for example in Fig. 23, it was not necessary to generate additional samples for the training process to be effective.

Figure 23: Network Input Example.

4.2.5 Training & Optimization

The same model architecture and training parameters were used for the UAV images as for the satellite images.
The plots in Fig. 24 illustrate the evolution of the two main metrics during U-Net training:

- Graph 1 shows training and validation accuracy across epochs. Training accuracy starts at ~0.26, rises rapidly within the first ten epochs to ~0.57, and gradually converges around 0.63. Validation accuracy remains slightly higher throughout, indicating a stable learning process without significant overfitting.
- Graph 2 presents the mean IoU for training and validation. The initial IoU is ~0.08 on the training set and ~0.19 on the validation set. By the end of training, the training IoU reaches 0.37 and validation IoU 0.30, confirming that the model gradually improves its ability to segment individual classes.

Final evaluation on the test set yielded an accuracy of 0.6371 and a mean IoU of 0.2985, demonstrating that the U-Net achieved satisfactory performance on this UAV dataset.

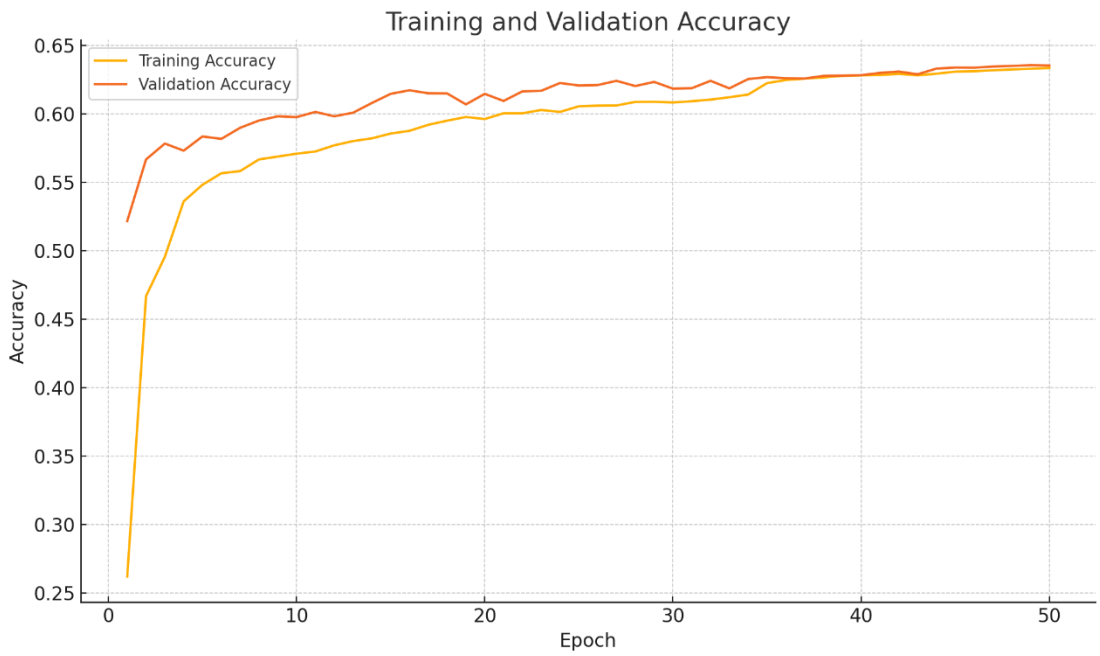

Graph 1

Graph 2

Figure 24: Training Results for different metrics.

Further improvements can be expected with larger training datasets, hyperparameter fine-tuning, or integration of complementary data sources. The complete training code is included in the Appendix (Listing 4).

CHAPTER 5

Experimental Results

This chapter presents the experimental results and the subsequent applications of training on UAV images. In Graph 1 (see Fig. 25), the Intersection over Union (IoU) metric is shown for each class.

We observe that for the well-defined classes:

- road, and
- building,

the network achieves fairly good performance.
However, for the vegetation classes, due to their high similarity, performance is less satisfactory. In Graph 2, where the results are displayed as a confusion matrix, we see that the diagonal elements—which represent correct classifications—are the ones expected to have the highest values.

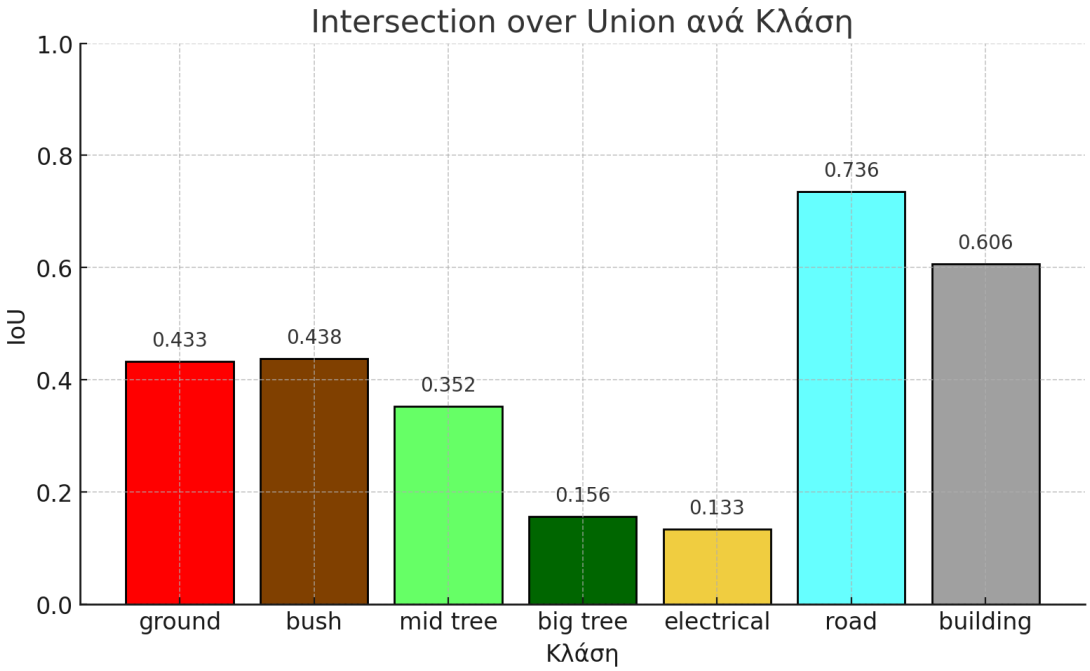

Graph 1

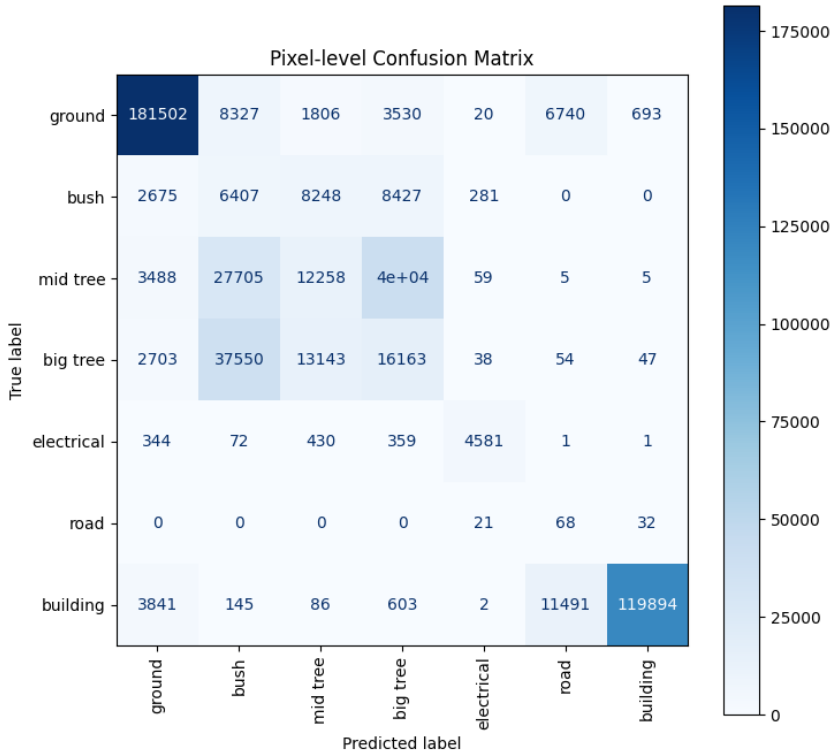

Graph 2

Figure 25: Other Graphs of training metrics.

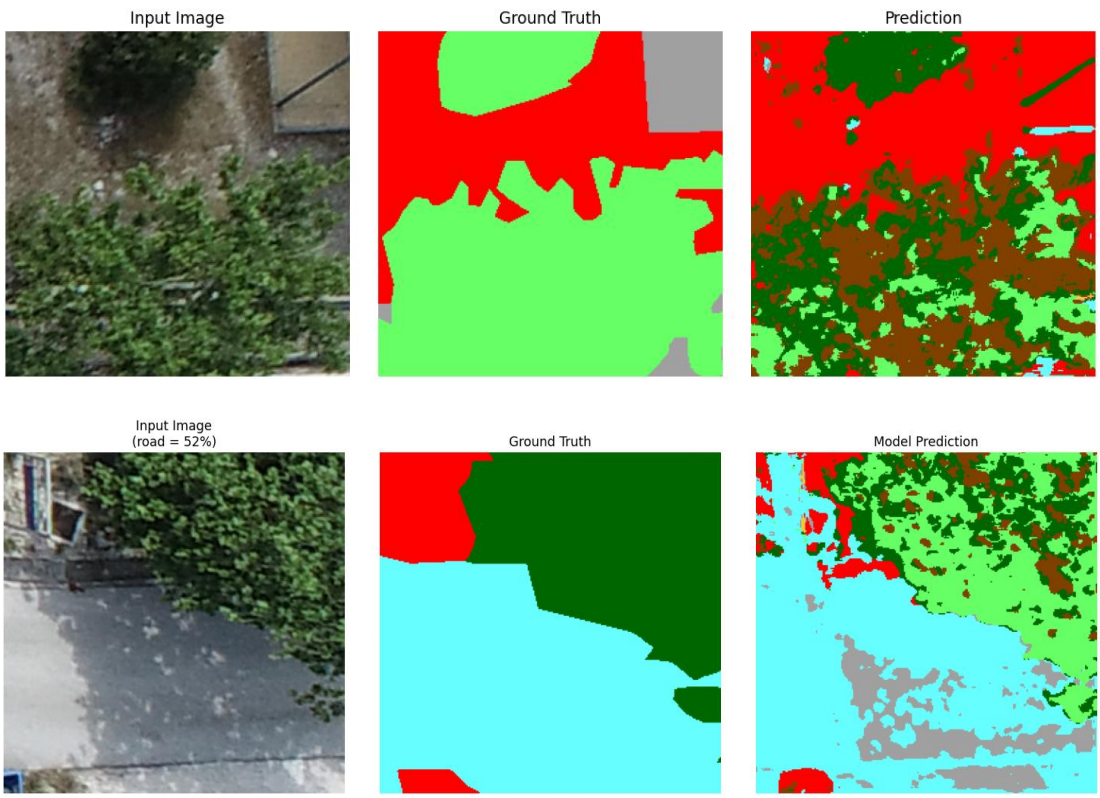

Figure 26: Network Output Examples.

The final output of the trained network when used for prediction is shown in Fig. 26. On the left is the 256×256 input image, in the middle the labeled mask, and on the right the prediction/output of the network. Fig. 27 shows the final model output after stitching the patches into a 12×12 layout, producing a full-resolution mask of the same size as the original input image. The stitching lines are clearly visible but without noticeable seam artifacts, while the main classes are represented correctly. Small uncertainties can be seen at class boundaries—especially between roads and buildings—indicating potential for improvement in edge post-processing. Overall, the patch-stitching achieves a coherent segmentation, ready for subsequent fire-risk map generation.

Figure 27: Stitching Results.

To improve the spatial consistency of the predictions, a median filter with a 41×41 pixel window was applied to the raw stitched prediction. The median filter is a simple, non-linear image processing technique. A k×k window (41×41 in this case) slides over the image, collecting the pixel values within the window. These values are sorted, and the median value replaces the central pixel. In this way, each new pixel is derived from the median of its neighbors, without averaging or weighting.

As shown in Fig. 28, this post-processing step eliminates many small, sporadic predictions (*salt-and-pepper noise*), enhancing the continuity of regions. For example, large ground areas become straight and uninterrupted, while the boundaries between road and bush become sharper.

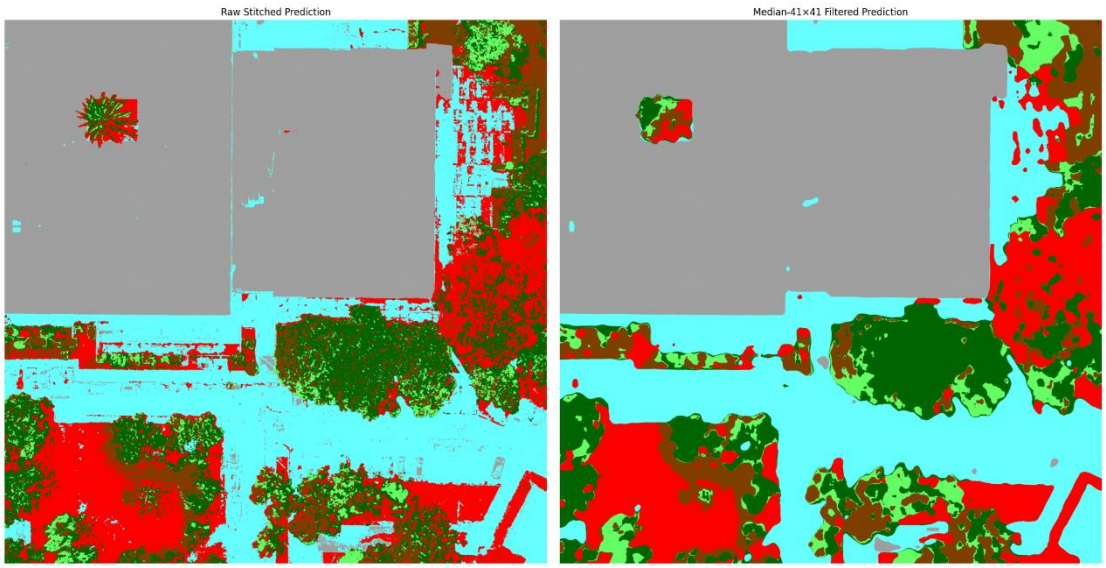

Figure 28: Filter Application.

The impact of the median filter on object detection accuracy is illustrated in **Graph 1 (see Fig. 29)**, which presents IoU values for each class, before and after applying a 41×41 spatial median filter on the model output. IoU is a critical evaluation metric for overlap between predicted and ground-truth labels, and is thus directly linked to the quality of spatial information.

As shown, the application of the filter had a positive effect on most classes, improving prediction clarity and reducing boundary noise. More specifically:

- **Ground**: IoU increased from 0.379 to 0.413, indicating better unification of ground surfaces.
- **Bush**: although relatively underrepresented, improved slightly but clearly (from 0.155 to 0.183).
- **Mid tree**: increased from 0.159 to 0.228, showing the highest relative improvement, suggesting that the filter reduces fragmented predictions in semi-continuous tree areas.
- **Big tree**: already performing reasonably well (0.404), improved further to 0.435.
- **Road**: showed a notable improvement (from 0.780 to 0.814), which is particularly important for mapping applications.
- **Building**: already very high IoU values improved slightly from 0.937 to 0.949, confirming the stability of predictions in areas with strong geometric structures.
- **Electrical equipment**: remained at zero, due to its extremely low representation in the dataset and, in particular, its absence in this specific image (to be shown in a later example). Consequently, filtering had no effect on this class.

In summary, the results demonstrate that even a simple spatial median filter can yield significant qualitative improvements in the generated masks—particularly for heterogeneous or noisy classes—without negatively affecting the highly predictable categories. This step offers minimal computational cost but considerable benefit for the post-processing of outputs in computer vision systems.

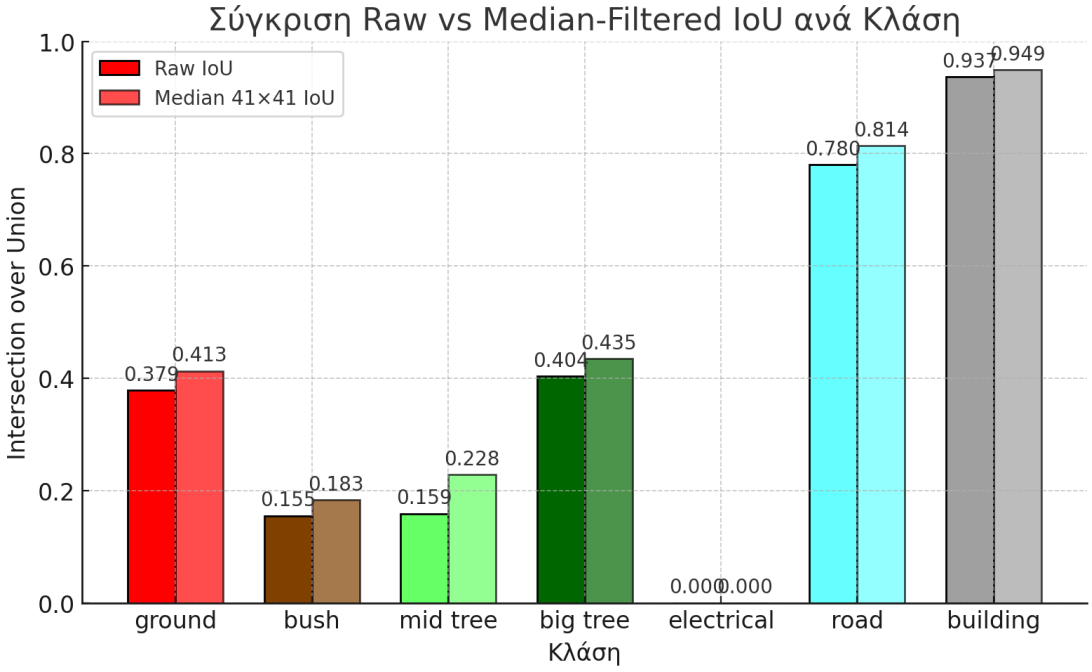

Graph 1

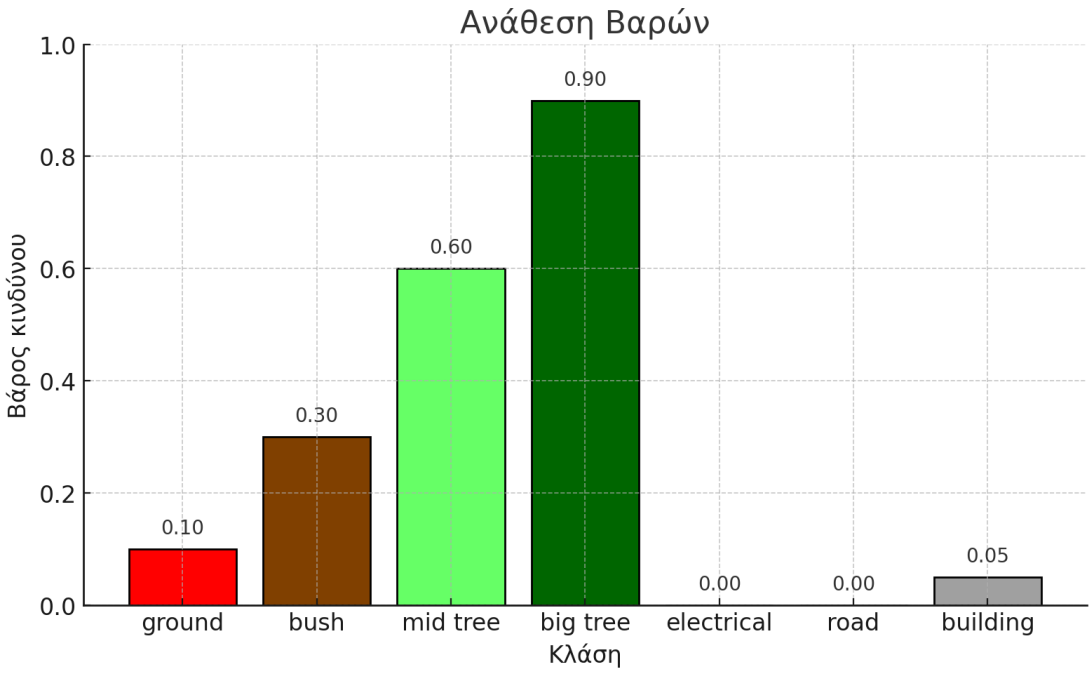

Graph 2

Figure 29: Example of IoU improvement and weight assignement.

Next, each predicted label class was assigned a corresponding risk index (weight), as shown in the “Weight Assignment” chart (Graph 2). Classes associated with medium and high fire hazard, such as mid tree and big tree, were given higher weights (0.60

and 0.90 respectively), while road and electrical were treated as neutral (0.00). This differentiated weighting scheme makes it possible to translate risk intensity directly into spatial representation, with a clear pixel-level gradation.

To further improve visual coherence, a median smoothing filter with a 9×9 pixel window was applied to the raw danger map, suppressing small sporadic anomalies (see Figure 30). In the “Raw Danger Map” (top right), small patches of high-risk pixels are scattered across shrub and tree areas, whereas in the “Smoothed Danger Map” (bottom left), these appear as more cohesive zones with smoother transitions. Finally, the “Overlay” (bottom right) projects the color-coded risk layer on the original UAV image, clearly highlighting the most hazardous areas (in warm tones) relative to their surroundings. This visual representation facilitates quick interpretation of the danger map and supports real-time decision-making.

It is evident that in areas dominated by pine or eucalyptus trees, the danger level is indeed higher, while only a few regions exhibit system confusion or prediction errors.

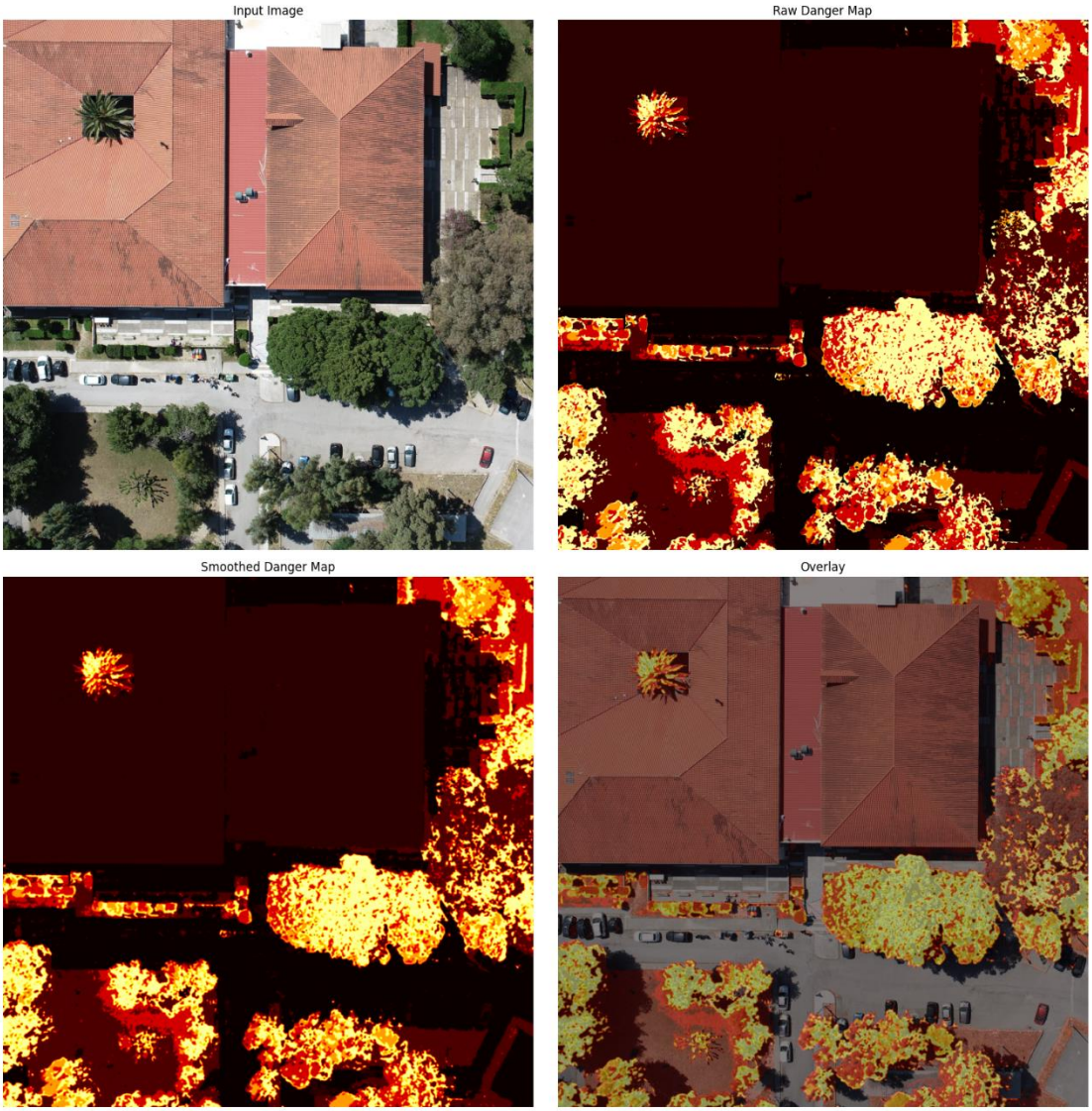

Figure 30: Resulting final risk-map.

Finally, Figures 31 and 32 illustrate the same process applied to the detection of high-voltage network infrastructure, specifically power lines.

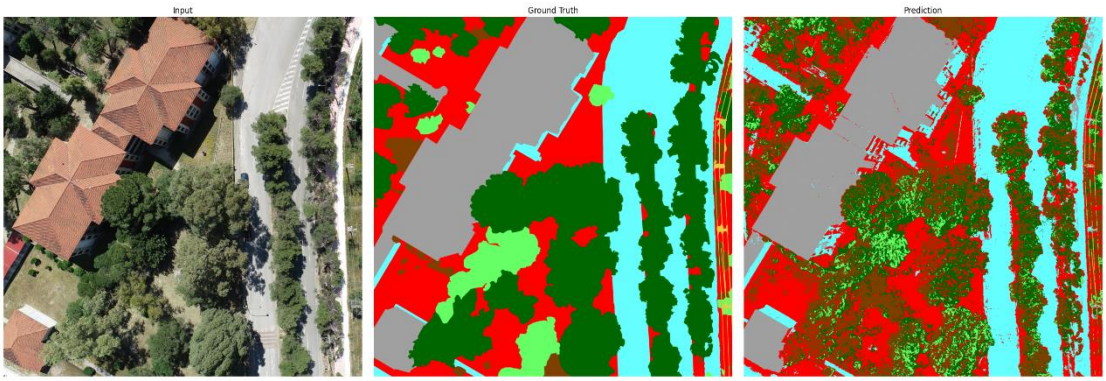

Figure 31: One more example.

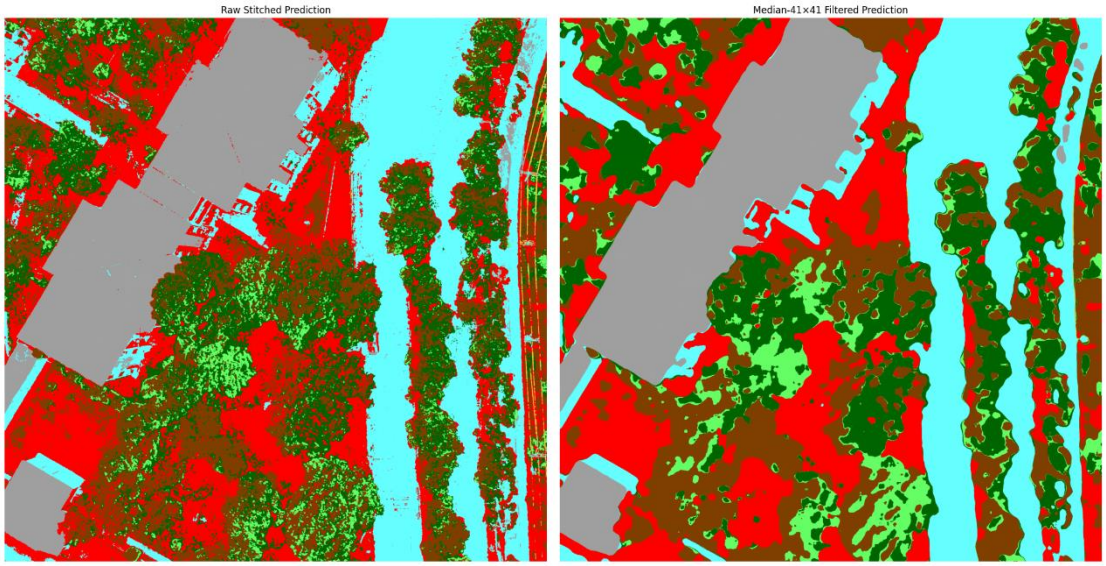

Figure 32: Filter Application.

In Graph 1 (Figure 33), IoU scores are presented once again, showing a notable improvement across all classes with the sole exception of **electrical**. The lack of improvement here can be explained by the nature of the objects in this class: electrical cables are extremely thin with very fine geometric structures. As a result, the spatial median filter fails to preserve them, treating them instead as isolated or discontinuous pixels and replacing them with the values of neighboring regions.

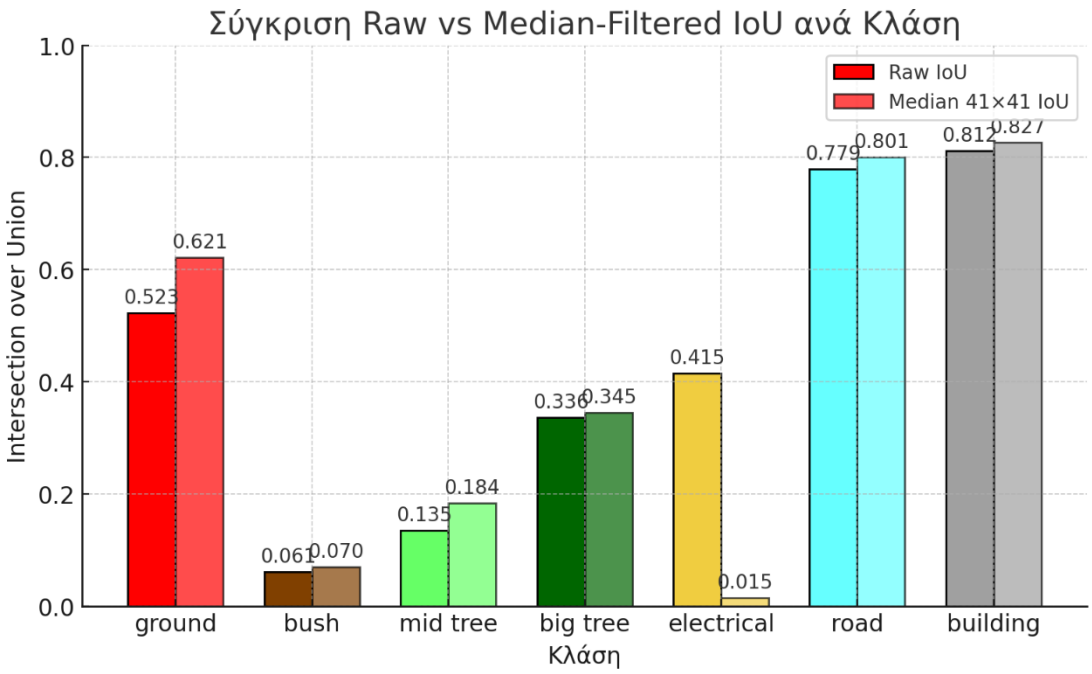

Graph 1

Figure 33: IoU before and after post processing.

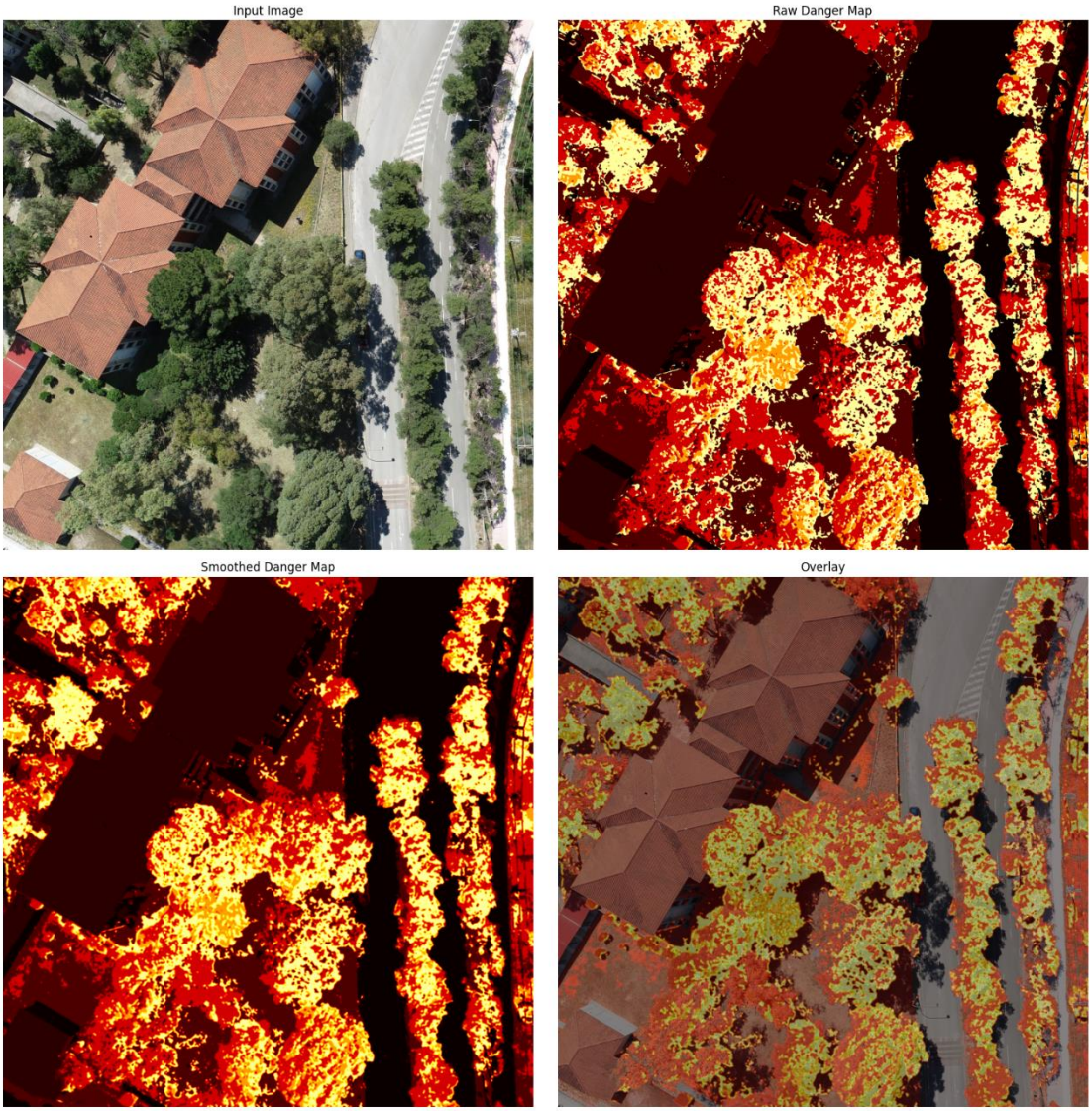

Figure 34: Final heat map.

Stepping back a few stages in the analysis (see Figure 31), a transformation is applied to the final classification output, where all pixels except those of the electrical class are set to black. This creates a binary mask that highlights only the regions identified by the system as belonging to that class. The result is shown in Figure 35, where electrical areas are depicted with a yellow overlay against a black background.

The generation of this mask is particularly useful in spatial hazard mapping applications, where the coexistence of power lines and vegetation represents a critical factor in preventing wildfires or network failures. More specifically, isolating the electrical class visually—by separating it from the surrounding environment—enables the precise localization of power lines and the evaluation of whether they are in close proximity to vegetation, such as medium or large trees. Such contact may compromise

line integrity in the presence of strong winds, falling branches, or sustained physical interference.

This approach allows the creation of a priority map for clearance or preventive intervention, supporting relevant authorities (e.g., fire department, utility operators, local government) in pinpointing the most hazardous zones. Thus, even if the electrical class achieves relatively low scores in conventional metrics (such as IoU), its targeted projection combined with georeferencing renders the system practically valuable in early prevention and recovery applications.

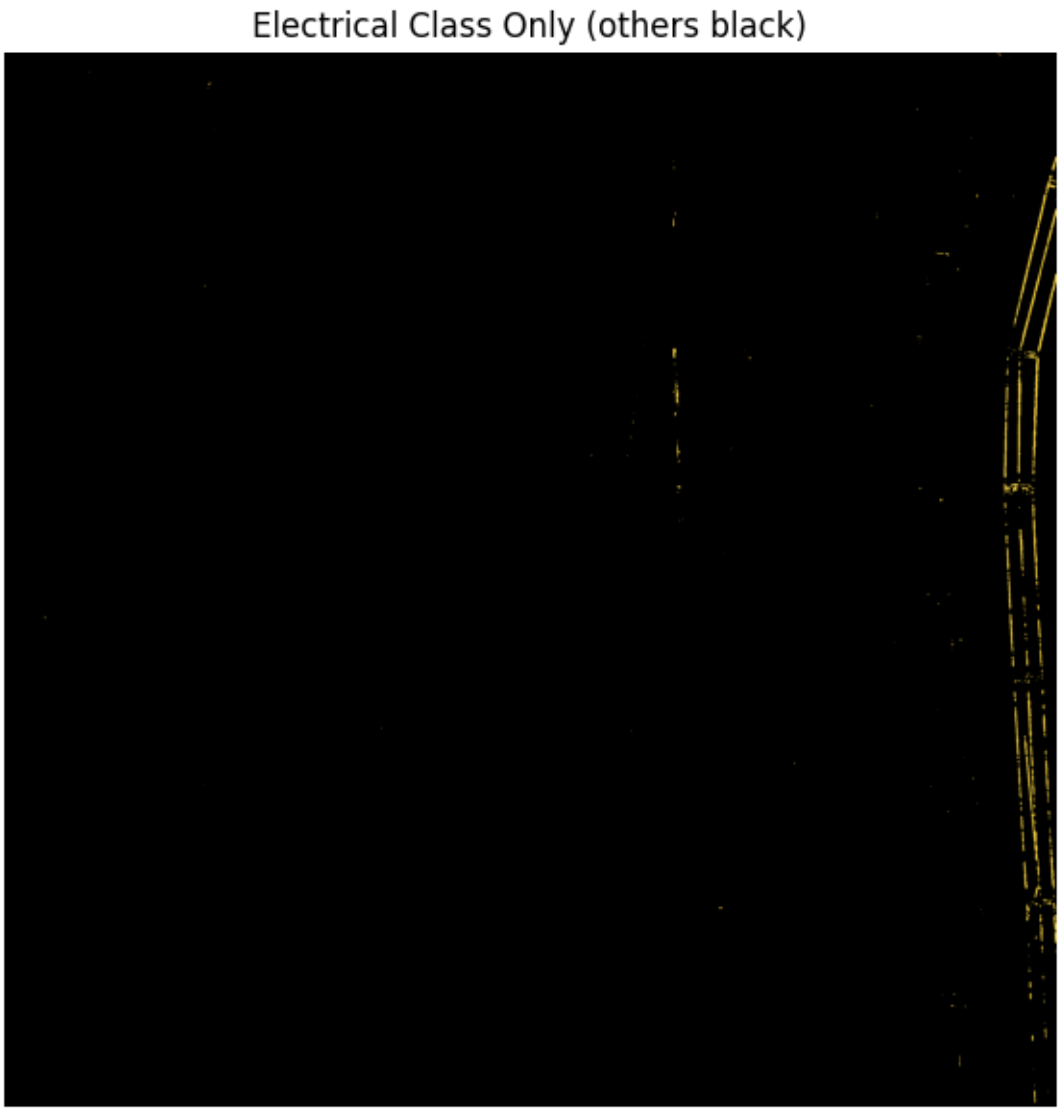

Figure 35: Mask containing only the class electrical pixels.

CHAPTER 6

Conclusion and Future Work

This thesis presented the implementation of a fully automated pipeline for generating wildfire hazard maps using exclusively UAV and satellite imagery, based on semantic segmentation with U-Net neural networks. The results, while moderate (final accuracy ~0.64, mean IoU ~0.30), demonstrate the feasibility of the method and its capacity to distinguish between key vegetation types, infrastructures, and roads.

The main limiting factors are those outlined in Section 4.2.1 *Limitations & Final Pipeline*, with the most significant being the size, quality, and representativeness of the dataset. Addressing these constraints—especially through expanding the dataset with additional UAV flights, incorporating more vegetation classes, improving labeling quality (larger and more complete masks), and employing advanced augmentation techniques—can be expected to yield significant improvements in performance metrics.

A promising direction for future research is the integration of the generated maps with dynamic indices based on meteorological data (temperature, humidity, wind), along with established fire risk models (e.g., FWI, RiskMap). Such a combination would enable more holistic and predictive hazard maps, supporting both prevention and timely response by fire services.

Finally, given the model's already mature segmentation performance, the next step is the full automation of the workflow—from UAV flight and image collection to the production of final hazard maps—through mission planning and streamlined data management pipelines. This would allow the platform to operate in near-real-time field conditions, offering an accessible and reliable tool for wildfire risk management.

Bibliography

[1] Z. Popović, S. Bojović, M. Marković, και A. Cerdà, “Tree species flammability based on plant traits: A synthesis,” Science of the Total Environment, vol. 800, p. 149625, 2021.

[2] G. Maria, E. Baccaglini, D. Brevi, M. Gavelli, και R. Scopigno, “A drone-based image processing system for car detection in a smart transport infrastructure,” in Proc. 18th Mediterranean Electrotechnical Conf. (MELECON), Limassol, Cyprus, 18–20 Apr. 2016.

[3] M. A. Finney, “FARSITE: Fire Area Simulator—model development and evaluation,” Res. Pap. RMRS-RP-4, USDA For. Serv., Rocky Mountain Res. Station, Ogden, UT, Mar. 1998.

[4] J. H. Scott και R. E. Burgan, “Standard fire behavior fuel models: a comprehensive set for use with Rothermel’s surface fire spread model,” Gen. Tech. Rep. RMRS-GTR-153, USDA For. Serv., Rocky Mountain Res. Station, Fort Collins, CO, Jun. 2005.

[5] H. E. Anderson, A photo guide to the 13 National Forest fuel models, Gen. Tech. Rep. INT-122, USDA For. Serv., Intermountain For. and Range Exp. Station, Ogden, UT, Apr. 1982.

[6] P. L. Andrews, “Current status and future needs of the BehavePlus fire modeling system,” Int. J. Wildland Fire, vol. 33, 2014.

[7] F. A. Albini, “Estimating wildfire behavior and effects,” Gen. Tech. Rep. INT-30, USDA For. Serv., Intermountain Res. Station, Ogden, UT, 1976.

[8] R. C. Rothermel, “A mathematical model for predicting fire spread in wildland fuels,” Res. Pap. INT-115, USDA For. Serv., Intermountain Forest and Range Exp. Station, Ogden, UT, 1972.

[9] R. C. Rothermel, “How to predict the spread and intensity of forest and range fires,” Gen. Tech. Rep. INT-143, USDA For. Serv., Intermountain Forest and Range Exp. Station, Ogden, UT, 1983.

[10] C. E. Van Wagner, “Conditions for the start and spread of crown fire,” Can. J. For. Res., vol. 7, pp. 23–34, 1977.

[11] T. L. Clark, M. A. Jenkins, J. L. Coen, και D. R. Packham, “A coupled atmosphere–fire model: convective feedback on fireline dynamics,” J. Appl. Meteor., vol. 35, no. 6, pp. 875–901, 1996.

[12] R. D. Ottmar και R. E. Vihnanek, Stereo photo series for quantifying natural fuels, Vols. I–VIa, PMS 830–838, Nat. Wildfire Coordinating Grp., Boise, ID, 1998–2003.

[13] C. S. Wright, R. D. Ottmar, και R. E. Vihnanek, Stereo photo series for quantifying natural fuels: Grassland, shrubland, woodland, and forest types in Hawaii, Gen. Tech. Rep. PNW-GTR-545, USDA For. Serv., Pacific Northwest Res. Station, Portland, OR, 2002.

[14] M. G. Bianchi και N. Defossé, “Fire dynamics in shrublands: a study of morphological traits and ignition,” Int. J. Wildland Fire, vol. 26, no. 8, pp. 725–734, 2017.

[15] V. Mola et al., “Interspecific variation in leaf-litter bed flammability: implications for ecosystem management,” Plant Ecol., vol. 215, pp. 757–766, 2014.

[16] X. Dimitrakopoulos και C. Papaioannou, “Flammability assessment of Mediterranean forest fuels,” Fire Safety J., vol. 36, pp. 171–183, 2001.

[17] T. Moranduzzo, F. Melgani, και A. Daamouche, “An object detection technique for very high resolution remote sensing images,” in 8th Int. Workshop on Systems, Signal Processing and Applications, May 2013, pp. 79–83.

[18] T. Viola και M. Jones, “Robust Real Time Object Detection,” in Proc. IEEE ICCV Workshop on Statistical and Computational Theories of Vision, July 2001.

[19] S. Liao et al., “Learning Multi-scale Block Local Binary Patterns for Face Recognition,” in Int. Conf. Biometrics (ICB), 2007, pp. 828–837.

[20] Hellenic Fire Service, “Annual Report on Forest Fires in Greece 2023,” Hellenic Fire Service, Athens, 2024.

[21] Panhellenic Wildlife Federation, “Impact of 2023 Wildfires on Fauna in Greece,” PWF Report, 2024.

[22] Institute for Soil Erosion and Water Management, “Post-fire Soil Erosion and Water Resource Impacts in Greece,” IS Erosion, 2024.

[23] Greek National Meteorological Service, “Storm Daniel 2023 Flood Report,” GNMS, 2023.

[24] NASA, “MODIS Instrument User’s Guide,” NASA Earth Observing System, 2022.

[25] NOAA, “VIIRS Product Guide,” National Oceanic and Atmospheric Administration, 2022.

[26] Hellenic Fire Service, “After-Action Review: Schinos Fire Incident 2023,” Hellenic Fire Service, 2024.

[27] Food and Agriculture Organization, “Global Forest Resources Assessment 2020 – Country Report: Greece,” FAO, Rome, 2020.

[28] National Forest Inventory of Greece, “Forest Cover Statistics 1990–2022,” Ministry of Environment and Energy, Athens, 2023.

[29] European Forest Institute, “Forest Zonation and Species Distribution in Mediterranean Europe,” EFI Technical Report 2019/05, 2019.

[30] European Space Agency, “Sentinel-2 User Handbook,” ESA, Noordwijk, 2015.

[31] NASA LP DAAC, “MODIS Land User’s Guide,” NASA, 2018.

[32] J. Long, E. Shelhamer, και T. Darrell, “Fully Convolutional Networks for Semantic Segmentation,” in Proc. IEEE Conf. on Computer Vision and Pattern Recognition (CVPR), 2015, pp. 3431–3440.

[33] O. Ronneberger, P. Fischer, και T. Brox, “U-Net: Convolutional Networks for Biomedical Image Segmentation,” in Medical Image Computing and Computer-Assisted Intervention (MICCAI), 2015, pp. 234–241.

Appendix

Παρακάτω παραθέτω έναν σύνδεσμο που ανακατευθύνει στο αρχείο με τα κομμάτια κώδικα σε κάθε εφαρμογή που προαναφέρονται.

https://github.com/argi4s/Thesis